Alma Mater Studiorum - Università di Bologna

DOTTORATO DI RICERCA

Ciclo XXI

Settore FIS/07

Monte Carlo Simulations of Novel Scintillator Detectors and Dosimetry Calculations

Dr. Sergio Lo Meo

Coordinatore Dottorato:
Chiar.mo Prof. F. Ortolani

Relatore:
Chiar.mo Prof. F. L. Navarria

Esame finale anno 2009

to ***Mariya and Sasha***

Acknowledgments

In primis, il Prof. F. L. Navarria per l'opportunitá che mi ha dato e per tutto cio' che mi ha insegnato.

Il Dr. Andrea Perrotta, "il piu' grande esperto di geometrie 3D presente nell'universo e in quelli ipotizzati", per le sue dritte illuminanti nei momenti piu' critici.

Il Dr. Nico Lanconelli, per il continuo e fondamentale aiuto.

Il Prof. R. Pani, per il prezioso supporto teorico e sperimentale necessario allo svolgimento di questo lavoro di tesi.

La Dr.ssa R. Pellegrini, la Dr.ssa M. N. Cinti ed in particolare ll Dr. P. Bennati, sempre presente, in qualsiasi ora del giorno e della notte, per fornirmi i dati necessari alle mie simulazioni.

Oltre ai doverosi "acknowledgments" professionali, ci tengo a ringraziare varie persone per la loro vicinanza affettiva.

Mia moglie Mariya per l'amore e la pazienza di questi anni.

Mia figlia Sasha, per la dolcezza e la gioia che mi trasmette nei momenti di maggior stanchezza.

I miei genitori, per il loro fondamentale sostegno in questo lungo periodo.

Contents

Introduction

Monte Carlo (MC) simulation techniques are becoming very common in the Medical Physicists community. Various general purpose MC codes, initially developed to simulate particle transport in a broad context, can be used also for modeling Single Photon Emission Computed Tomography (SPECT) and Positron Emission Tomography (PET) configurations [1]. As they have been designed for a large community of researchers, these codes are well documented and are available in the public domain. Several topics are addressed by MC in the Nuclear Medicine (NM) field, among them, in this study, we present the use of MC for optimization of SPECT imaging systems design and for dosimetry calculations.

Radiation plays a key role in the treatment of many cancer types and in medical diagnosis. Radiotherapy with radiation other than gamma and X-rays has become important based on the specific physical properties of alpha and beta-emitting radionuclides. A Technetium congener, Rhenium-188 (^{188}Re), is a promising candidate for radiotherapeutic production. In the first Chapter, we present results obtained on the radio-response of ^{188}Re-perrhenate in a panel of human tumor cell lines. Inhibition of cell proliferation, induction of micronuclei and apoptosis have been considered as measures to ascertain the sensitivity of the tumor cell to the β-emission of ^{188}Re. The dosimetry of ^{188}Re, used to target the different lines of cancer cells, has been evaluated by the MC code GEANT4 [2]. The simulations estimate the average energy

deposition/per event in the biological samples.

While the ^{188}Re beta emission is fundamental for therapeutic purposes [3], the gamma rays can be detected, by gamma-cameras, to evaluate the biodistribution of the radionuclide and for a real-time SPECT monitoring of regional drug concentration during radiation therapy. With the use of ^{188}Re for imaging purposes in mind, in the second Chapter we present a study of gamma-cameras based on planar scintillation crystals of Lanthanum Bromide doped with Cerium ($LaBr_3$:Ce). The simulation tests, by GEANT4, start from a radioactive decay source and halt when the scintillation photons reach the photomultiplier (PM). In the simulations, the boundary processes on all crystal surfaces are considered. Different $LaBr_3$:Ce crystal configurations are simulated in view of optimizing the gamma-camera performance.

The visual quality and quantitative accuracy of radionuclide imaging, however, often lacks anatomic cues that are needed to localize or stage the disease and typically has poorer statistical and spatial characteristics than anatomic imaging methods, such as an ultrasound system. These issues have motivated the development of a new approach that combines functional data from compact gamma cameras with structural data from ultrasound equipments. The aim is to develop a dual integrated portable camera able to acquire tomographic images obtained by using simultaneously ultrasound and scintigraphic techniques. In the third Chapter preliminary results obtained for the setup of the ECORAD collaboration are described, and some simulated results of the scintigraphic part of the system are shown.

Chapter 1

SCINTIRAD

1.1 Introdution

SCINTIRAD [4] is a multidisciplinary collaboration that aims at determining the radioresponse of ^{188}Re, a β^- and γ emitter used in metabolic radiotherapy. The response with cells "in vitro", the biodistribution in different organs of mice "in vivo", and the therapeutic effect on liver and other tumors induced in mice, have been studied. SCINTIRAD is based on a large scientific collaboration:

- The National Institute of Nuclear Physics (INFN) sections of Bologna, Roma 1, Roma 3 and Legnaro.
- Physics Dept. - Alma Mater Studiorum - University of Bologna.
- Experimental Medicine Dept. "Sapienza" University of Rome.
- Physics Dept., Biology Dept. - University of Rome 3.
- Physics Dept., Pharmacology Science Dept., Pathology and Veterinary Hygiene Dept., Oncology and Surgical Sciences Dept. - University of Padua.

- Natural Sciences Dept. - Shumen University (Bulgaria).
- Dept. of Technology and Health - Italian Istitute of Health (ISS).

^{188}Re is a promising candidate for application in NM [5]. While the beta emission is fundamental for therapeutic purposes, the gamma rays can be detected to evaluate the biodistribution of the radionuclide and for a real-time SPECT monitoring of regional drug concentration during radiation therapy. Hyaluronic Acid (HA) is a molecule already adopted as a suitable vector of chemotherapeutic drugs [6]. Technetium-99m HA (^{99m}Tc-HA) labeling procedure and biodistribution studies have been previously reported in literature [7]. HA has also been adopted as a vector for ^{188}Re and preliminary results on the effect of a ^{188}Re-perrhenate solution on a series of tumor cell lines obtained in vitro have been presented in [8].

The dosimetry of ^{188}Re used to target the different lines of cancer cells has been evaluated by a MC simulation based on GEANT4, and the preliminary results obtained are presented in Section 1.4.

1.2 Biological studies

Radiotherapy with radiation other than gamma and X-rays has become important based on the specific physical properties of alpha and beta-emitter radionuclides when conjugated with biologic molecules carrier, such HA, monoclonal antibodies, etc. As a result of tumor targeting, a cell-focused delivery of radiation is obtained compared to irradiation with sparsely ionizing gamma or X-rays, leading furthermore to the advantage of treating widely disseminated diseases as secondary or metastasis cancer.

A major factor in the failure of radiotherapy is represented by inherent or induced cellular radioresistance [9]. In fact, it is well established that different human tumor

types can differ greatly in their sensitivity to radiation [10]. Up to now, the intrinsic radiosensitivity has been evaluated in a large panel of human tumor cell lines after "in vitro" exposure to gamma or X-rays. Conversely, scanty data are available in the literature on the radioresponse of tumor cells after treatment with radiopharmaceuticals characterized by beta-emission. To gain this piece of information is particularly relevant considering that the radiosensitivity "in vitro" can predict the outcome of irradiation "in vivo".

Molecular mechanisms in which cell death is caused by beta-irradiation are not well understood and no data on beta-irradiation-induced apoptosis of cells derived from solid tumors are available in the literature. ^{188}Re, is a promising candidate for radiotherapeutic production and understanding the mechanisms of the radioresponse of tumor cells to ^{188}Re is of crucial importance as a first step before "in vivo" studies, where the same cells may be inoculated/injected in mice and then treated with a biomolecule conjugated with ^{188}Re. In this respect, since in most malignant cell types the specific membrane receptor CD44 is typically overexpressed [11], HA, which binds CD44, can be successfully exploited as ^{188}Re carrier.

1.2.1 Rhenium-188

Rhenium is a chemical element with the symbol "Re" and atomic number 75. Rhenium (Latin Rhenus meaning "Rhine") is the next-to-last naturally occurring element to be discovered and the last element having a stable isotope. Its isotope, ^{188}Re, has chemical properties similar to the widely used congener ^{99m}Tc, this permits to use all the information on the biodistribution of ^{99m}Tc-radiopharmaceutical to be used for the research of effective ^{188}Re-radiotherapeuticals.

^{188}Re decays [12] to ^{188}Os (70%) or ^{188}Os* (30%) with a half-life of about 17 hours, via the emission of a β-ray, the most frequent transition (70%) having a maximum

energy of 2.12 MeV (0.78 MeV average energy). At the maximum energy, the electron is absorbed within a radius of 11 mm in biological tissues. In addition, $^{188}Os^{*}$ emits promptly (0.69 ns) a γ-ray, mainly in the line at 155 keV but with the photon spectrum extending up to about 2 MeV. In 15.6 % of the ^{188}Re decay chains, a 155 keV photon is emitted.

1.2.2 Studies in "vitro"

Cells were seeded at appropriate concentrations in 96-multiwells (4 wells/cell line; 100 μl/well) [8]. Cell cultures are deposited inside the (darkest) wells of the experimental setup, as shown in Fig. 1.1.

Figure 1.1: A picture of the wells used to assess biological response to ^{188}Re of a set of human tumor cell lines. The rectangle indicates the well geometry used in the MC simulation (see Section 1.4).

Active wells are interleaved by empty holes filled with water, acting as absorbing medium, to simplify the evaluation of the dose. Neoplastic cells of different histotypes (H460 lung cancer cells, U87 glioblastoma, LnCaP prostate tumor cells) are used. The data (Fig. 1.2) are presented as percentages of viable cells, in cultures ^{188}Re-exposed, with respect to untreated ones.

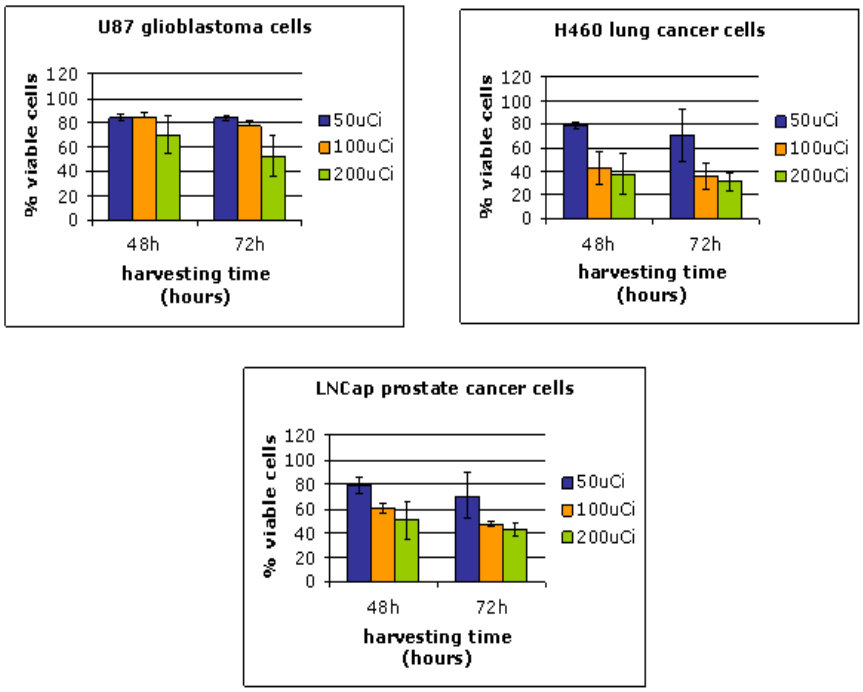

Figure 1.2: Percentages of viable cells in tumor cell lines exposed for 48 or 72 h to ^{188}Re-perrhenate.

After 48 or 72 h, by using specific initial activities ranging from 18.5 to 74 GBq/l, the evaluation is done by means of a recognized test for cytotoxicity which measures mitochondrial metabolism in the entire cell culture: MTT [1] assay [16]. Inhibition of cell proliferation, induction of micronuclei and apoptosis have been considered as measures

[1] 3-(4,5-dimethylthiazol-2-yl)-2,5-diphenyltetrazolium bromide.

to ascertain the sensitivity to the β-emission of ^{188}Re. ^{188}Re-perrhenate treatment clearly indicates that the different tumor cells tested show different sensitivities. Radioresistance is characteristic of many different tumor types, among them glioblastomas are considered particularly radioresistant and long-term survivors with this diagnosis are very rare [17].

U87 glioblastoma cells showed about 20% reduction in cell viability (compared to untreated cultures, as shown in Fig.1.2) at both 48 and 72 h harvesting times. The maximum cellgrowth inhibition leading to 45% reduction of the cell viability is obtained after 72 h radiation exposure with initial specific activity of 74 GBq/l. On the contrary, both H460 and LnCap show a higher sensitivity to beta emissions of ^{188}Re and this is particularly visible at 72 h harvesting time.

As a next step, the relationship between cell death assessed by the MTT assay and the induction of apoptosis, a process that removes highly damaged cells from the replicative pool to maintain genome integrity, is checked. Cells are fixed, either in absolute methanol for 30 min and stained with 2.5 mg/ml DAPI[2] or in 4% paraphormaldeide and processed for the TUNEL[3] assay [18], in which the terminal deoxynucleotidyl transferase binds to 3'-OH ends of DeoxyriboNucleic Acid (DNA) fragments generated in response to apoptotic signals and catalyses the addition of biotin-FITC-labeled deoxynucleotydes[4]. Then the cells are exposed 48 h to 74 GBq/l ^{188}Re-perrhenate and the results show that U87 (Fig. 1.3) are extremely resistant to the induction of apoptosis. On the contrary for H460 and LnCap cells. In the graph of the Fig. 1.3 are reported the frequency of apoptotic cells induced after treatment ($t-test$: * $P < 0.05$; ** $P < 0.01$).

[2]4'-6-Diamidino-2-phenylindole (DAPI) is known to form fluorescent complexes with natural double-stranded DNA, showing a fluorescence specificity for AT, AU and IC clusters.

[3]Terminal deoxynucleotidyl Transferase Biotin-dUTP Nick End Labeling.

[4]Fluorescein isothiocyanate (FITC).

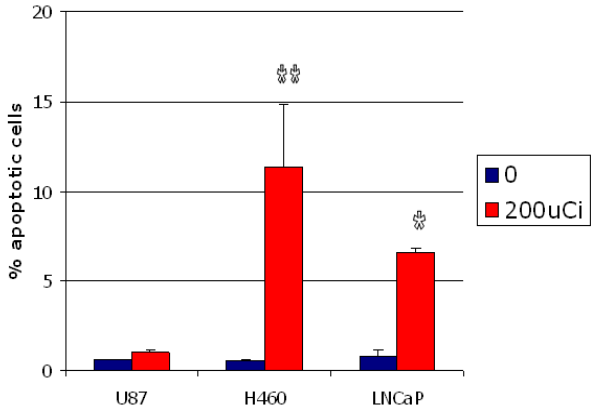

Figure 1.3: Frequency of apoptotic cells induced after treatment.

To asses induction of micronuclei (MN) in binucleated cells (BNC), cells were incubated for 48 hours in the presence of ^{188}Re and 3 μg/ml Cytocahlasin-B. The frequency of ^{188}Re-induced MN is reported in Fig. 1.4, showing a higher sensitivity of U87 glioblastoma cells. $(t-test$: $*p < 0.05$; $**p < 0.01)$

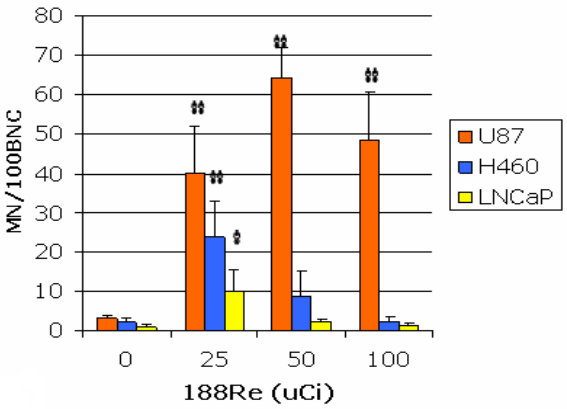

Figure 1.4: MN Frequency for BNC.

In conclusion, the preliminary results discussed here, indicate that cell lines established from lung and prostate cancer are particularly sensitive to ^{188}Re. In "vitro" studies, as shown by U87 glioma cells, citotoxicity is correlated with micro nuclei induction. Cells sensitive to ^{188}Re died through an apoptotic mechanism, as observed in H460 and LNCaP sensitive cells.

To estimate the total dose absorbed by the biological cells, a computation of the average dose per ^{188}Re decay, by using GEANT4 simulations, is described in Section 1.4.

1.2.3 Studies in "vivo"

The biodistribution studies are carried out in female BALB/c mice (a mice variety) by intravenous administration of ^{188}Re-HA. Thereafter mice are sacrificed at different time-points and selected tissues are excised, weighted and counted by a gamma counter. The activity of the tissue samples is expressed as % injected dose (ID)/ g of tissue. Four groups of three mice are i.v. administered with 4.62, 9.25, 18.5, 37.0 MBq of ^{188}Re-HA. Hepatic and spleen accumulation (Fig. 1.5), indicates that HA can be considered a suitable vector for the delivering of ^{188}Re in these organs. The liver-absorbed dose for each group is calculated using the formula:

$$D_{rad} = 1.44 \cdot \frac{A_0}{m} \cdot T_e \cdot \sum_i \Delta_i \cdot \Phi_i(t \leftarrow s) \tag{1.1}$$

Where: A_0= Activity (MBq), m=mass (g), T_e=effective time, $\Delta_i = N_i \cdot E_i$ (N_i=number of particles per nuclear transformation and E_i = energy of the radiation in MeV), and $\Phi_i(t \leftarrow s)$ = fraction of absorbed energy by the target organ from the source organ [14] [15]. The absorbed dose, according to eq. 1.1, for each group has been calculated to be 38.6, 73, 154, and 309 Gy respectively [13].

As a next step, the changes for spleen and liver weight, after mice injection of tumor cells (50000 Hepatic Metastasis M5076 cells per mouse) have been studied. The ^{188}Re-HA treatment, with for 60 or 120 μCi, after some days (from 7 to 18) causes death of tumor cells and consequently a weight decrease of mice spleen and liver (Fig. 1.6 and Fig. 1.7).

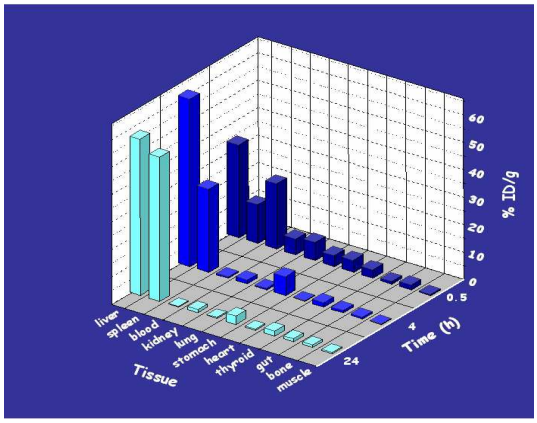

Figure 1.5: Biodistribution "in vivo".

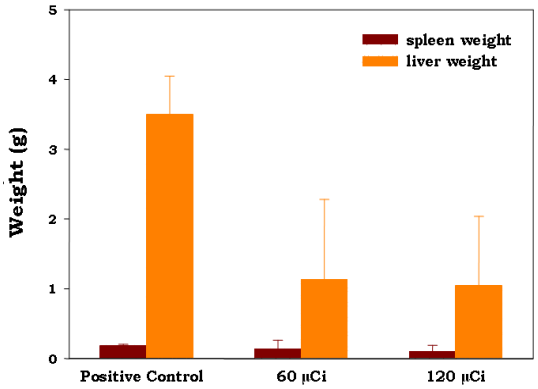

Figure 1.6: Spleen and liver weight test.

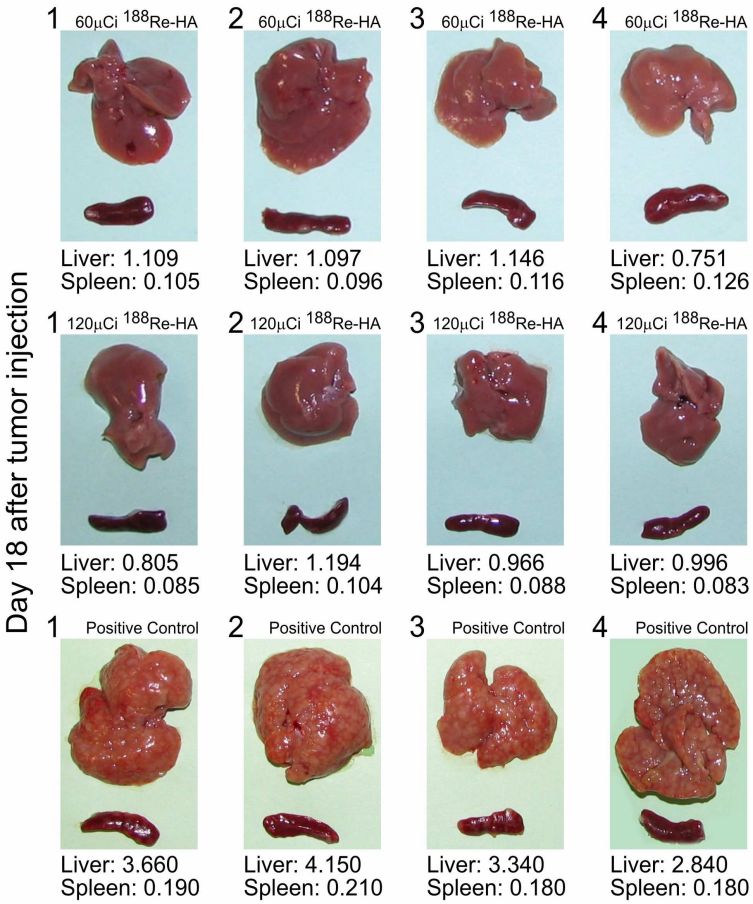

Figure 1.7: Spleen and liver weight after 18 days from tumor injection.

In conclusion, ^{188}Re has been conjugated with HA to perform biodistribution studies "in vivo" mainly showing hepatic and spleen accumulation with respect to other organs and consequently tumor reduction in mice spleen and liver.

1.3 GEANT4 overview

The acronym "GEANT" has been invented in the 1970's to name a code that simulated GEometry ANd Tracking for particle physics experiments. The first widely-used released version of the code, GEANT3, was written in FORTRAN and used several, at the time well-established, physics routines to model the physics of the interactions. As the complexity of the code kept increasing, object-oriented techniques have been opted for instead, as this seemed to be the most efficient way to maintain the transparency of the code without compromising its performance. At that point it has been also decided that the program would be given the form of a toolkit allowing the user to easily extend the components of all domains. This new phase of development led, in 1998, to the first production release of GEANT4, a C++ program that nowadays begins to be adopted by fields other than particle physics, such as space science and medical physics [19]. For the work presented in this Chapter, we use GEANT4 (version 4.7.1).

There are two landmarks for defining the geometry of a setup in GEANT4: the "World" volume and the internal reference frame of the simulation. The "World" volume is conceived as the volume that includes all the three-dimensional space that the simulation has to consider. The internal reference frame of GEANT4 is a cartesian system that has its origin at the centre of the "World". The other volumes are created and placed inside the "World" volume. When all volumes are thus placed, they are assigned materials. These are defined as elements or compounds. Compounds are defined by their atomic composition as given by a chemical formula or weight fractions, their density at a given temperature and pressure.

Once this is done, GEANT4 will track the particles through the system (following the definition of physics processes) until they stop, decay or are transported beyond the limits of the "World". The generation of the primary event can be done using the G4ParticleGun class or G4GeneralParticleSource (GPS) [20], which create a beam of

particles by defining their type, position, direction of motion and kinetic energy. The simulation proceeds by steps and the purpose of the implementation of the physics is to decide where these steps take place and which interactions are to be invoked at each step. This is done by using pseudo-random numbers which are uniformly distributed in the interval (0,1) to calculate the mean free path or interaction length for each interaction that the particle is allowed to undergo. The interaction that proposes the shortest mean free path is chosen.

In GEANT4 a random number generator is a distribution associated to an "engine". To chose and to use these "engines", the HEPRandom module, originally part of the GEANT4 kernel and now distributed as a module of CLHEP [21], is used. The HEPRandom module consists of classes implementing different random "engines" and different random "distributions". The class HepRandomEngine is the abstract class defining the interface for each random engine. For our purposes we have used the RanecuEngine [22]. The algorithm for RanecuEngine is taken from the one originally written in FORTRAN77 as part of the MATHLIB HEP library. The initialization is carried out using a multiplicative congruential generator using formula constants of L'Ecuyer [23]. Seeds are taken from a seed table given an index, the getSeed() method returns the current index of seed table. The setSeeds() method will set seeds in the local SeedTable at a given position index (if the index number specified exceeds the table's size, [index%size] is taken). Except for the RanecuEngine, for which the internal status is represented by just a couple of longs, all the other engines have a much more complex representation of their internal status. The status of the generator is needed, for example, to be able to reproduce a run or an event in a run at a given stage of the simulation. RanecuEngine is probably the most suitable engine for this kind of operation, since its internal status can be fetched/reset by simply using getSeeds()/setSeeds and this is the reason why we have used this engine.

In GEANT4 the step length can also be restricted to preserve precision or to prevent the particle from crossing a boundary in the geometry in a single step. The user can also request a maximum allowed step in the calculations. This latter option has not been used in the runs described here but instead the calculations have been determined only by the properties of the physics implementation. The processes taken into account in the present application are only the electromagnetic ones and nuclear decays.

In GEANT4 code, photons and secondary electrons are, however, generated only above a given kinetic energy threshold ("production cut-off"). This is done as to avoid the production of a large number of secondary particles (tipically for ionization and bremsstrahlung processes), which would deteriorate the performance of the simulation without enhancing the accuracy of the calculations. These thresholds should be defined as a distance, or range cut-off, which is internally converted to an energy for individual materials. The range threshold should be defined in the initialization phase using the SetCuts() method of G4VUserPhysicsList. In the present study, the range cuts for photons and electrons are fixed to 600 nm, much lower than the average height of culture cells (6 μm) simulated (see Section 1.4). Using 600 nm, the energy threshold for electrons and gamma in air, in water and in tissue is 990 eV.

GEANT4 uses Condensed History Technique (class 1 algorithms) that has been introduced by M. Berger in the early sixties [24]. In this technique, many track segments of the real electron random walk are grouped into a single "step". The cumulative effect of elastic and inelastic collisions during the step are taken into account by sampling energy and direction changes from appropriate multiple scattering distributions at the end of the step. This approach is justified by the observation that the changes of the electron state in a single collision are usually very small and fails when this condition is not satisfied (at very low energies).

In the 4.7.1 GEANT4 version, there are two models for electromagnetic physics:

the "standard" model and the "low-energy" model. The low-energy electromagnetic physics package [25], used for our dose calculation, is an extension of the standard physics code and uses shell cross section data rather than their parametrizations (as they are used in the standard model). A lowest validity limit of 250 eV was chosen to allow for the treatment of characteristic K-shell emission down to Z=6. The model covers the interactions of photons and electrons in materials with atomic number between 1 and 100. This package does not provide a new implementation of processes induced by positrons. They are treated by the same classes as in the standard electromagnetic physics package. The extended classes of the model treat the following interactions: Compton scattering, Rayleigh scattering, photoelectric effect, ionisation and bremsstrahlung. The model also provides implementations for atomic relaxation (fluorescence and Auger electrons not included in the "standard model"). The implementation of all processes is done in two phases: calculation of the total cross sections and generation of the final state. Both phases are based on data from the following libraries: Evaluated Photon Data Library (EPDL) [26], Evaluated Electron Data Library (EEDL) [27] and Evaluated Atomic Data Library (EADL) [28]. The energy dependence of the total cross section is derived for each process from the evaluated data libraries. The total cross-section at a given energy is calculated by interpolation between the closest lower and higher energies for which data are available [29].

For nuclear decays, GEANT4 provides a G4RadioactiveDecay class to simulate the decay of radioactive nuclei by α, β^+, and β^- emission and by electron capture (EC). The simulation model is empirical and data-driven, and uses the Evaluated Nuclear Structure Data File (ENSDF)[30] for information on:

- nuclear half-lives,

- nuclear level structure for the parent or daughter nuclide,

- decay branching ratios,
- the energy of the decay process.

If the daughter of a nuclear decay is an excited isomer, its prompt nuclear de-excitation is treated using the G4PhotoEvaporation class [31].

1.4 Dose calculation

1.4.1 Simulation setup

The experimental setup is reproduced using a simulation based on the GEANT4 MC program (Fig. 1.8).

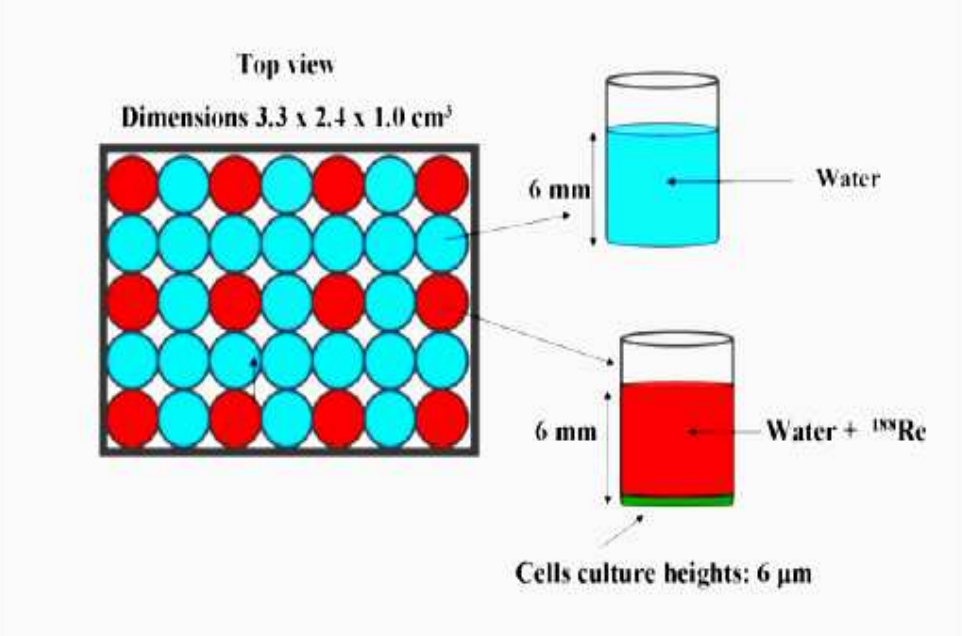

Figure 1.8: The modellization used for the simulation of the experimental setup.

It consists of a grid of 5×7 cylindrical wells disposed adjacent to each other, as in the real experiment. Wells are 9 mm high, with a 3.5 mm inner radius and 4.5 mm outer radius. The inner volume (6 mm high) is filled either with water, or with a solution containing water and ^{188}Re. In the simulation setup, the cells in the top three rows are filled with a solution with an initial activity of, respectively from top to bottom, 50, 100 and 150 μCi/cc. In the wells containing the radioactive solution, the 6 μm average height layer at their bottom represents the biological material which is irradiated. Figures 1.9 and 1.10 show the simulation setup by GEANT4.

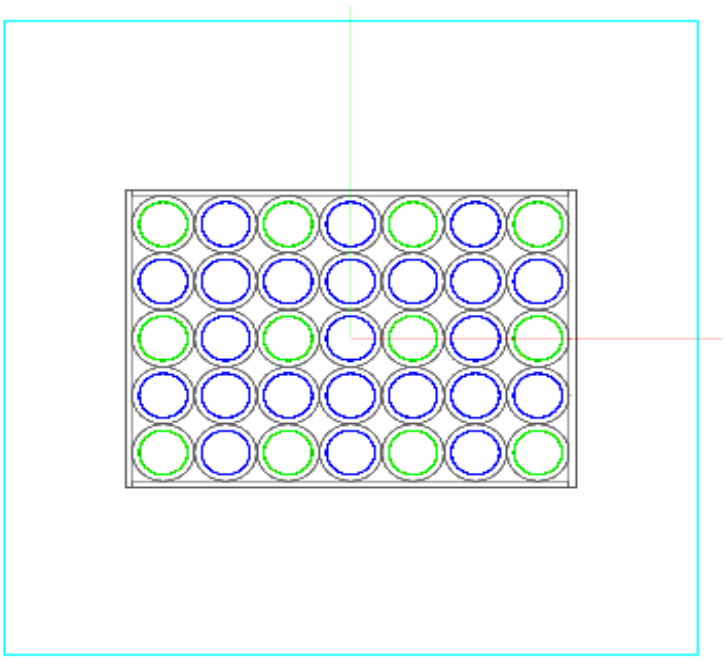

Figure 1.9: GEANT4 simulation setup (front view).

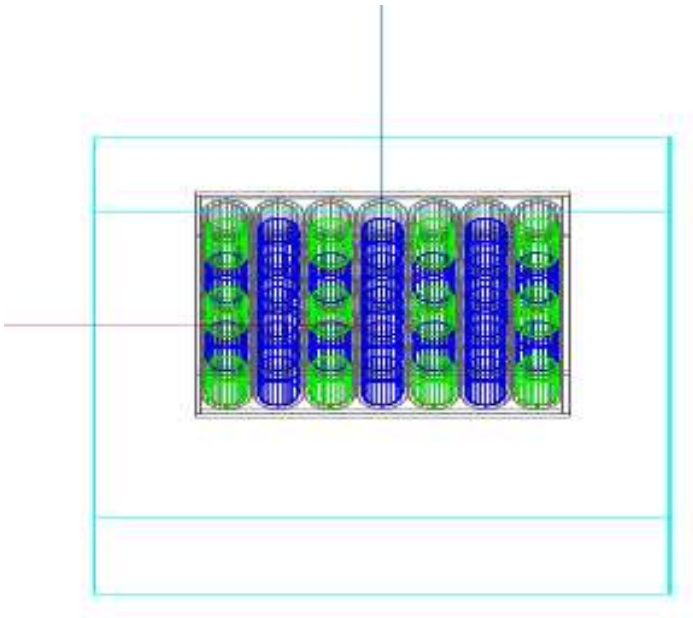

Figure 1.10: GEANT4 simulation setup (3D view).

1.4.2 Cross checks

Some cross checks are performed to verify the correct working of the simulation setup with respect to theoretical predictions,.

For the first check, 10^3 electrons with energy of 2.12 MeV (maximum energy of beta particle in ^{188}Re decay) are emitted in negative z-direction from a circular section (see Fig. 1.11) at half of the cylindric well. The energy deposition is given by:

$$\Delta E = (-\frac{dE}{dz})_{avg} \cdot \Delta z \tag{1.2}$$

where Δz is the depth along z direction, and $(-\frac{dE}{dx})_{avg}$ is the average Stopping Power, function of energy and type of the particle considered and function of the material used. In this check, we have water (3 mm) and tissue (6 μm). The ratio (R_{dep}), by Eq.

1.2, between the energy deposited in the tissue and that deposited in water is given by:

$$R_{dep} = \frac{\Delta z_{tissue}}{\Delta z_{water}} \tag{1.3}$$

By using the values of the depths simulated we have: $R_{dep}^{theor} = 2.0 \cdot 10^{-3}$. The value obtained by MC is an energy deposition (1.3 ± 0.1) MeV in tissue and (606.1 ± 0.6) MeV in water; therefore is $R_{dep}^{MC} = (2.2 \pm 0.2) \cdot 10^{-3}$, in a good agreement with the theoretical value.

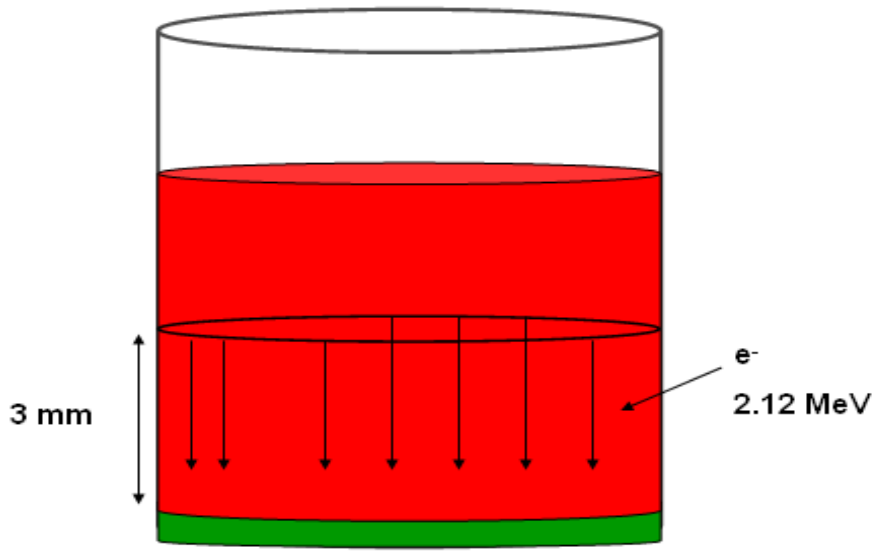

Figure 1.11: First check of simulation setup.

For the second check, we use methods for the decay of ^{188}Re, with its specific lifetime and spectra of decay products, included in GEANT4 (see Section 1.3). Figure 1.12 shows a decay visualization obtained by GEANT4. The average value and the maximum value obtained are in good agreement with literature data [12]. ^{188}Re decays and the products (photons, electron and anti-neutrino) are propagated inside the

simulated material. In Fig. 1.12, ^{188}Re decays β^- into $^{188}\text{Os}^*_{2,3}$ that decays promptly into the first excited state $^{188}\text{Os}^*_{2,5}$ and a 931 keV photon. $^{188}\text{Os}^*_{2,5}$ decays into ^{188}Os and a 155 keV photon.

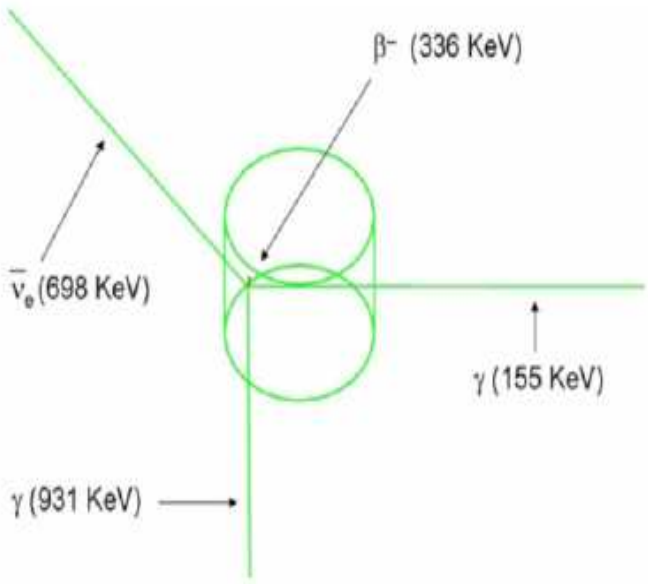

Figure 1.12: Example of a decay simulated with GEANT4.

Figure 1.13 shows the ^{188}Re β- spectrum from the GEANT4 simulation. Over the typical β^- spectrum it is possible to see the internal conversion picks. In fact, the gamma decay rays, typically 155 keV, can be absorbed by electron shells. These electrons are emitted with energy gives by:

$$E_{e^-} = E_\gamma - E_b \tag{1.4}$$

where E_b is the binding energy of the atomic shell (K,L,M). Figure 1.14 shows with more precision the 152 keV (shell M), the 142 and 144 keV (different levels of L shell) and finally the 81 keV (K shell) peaks.

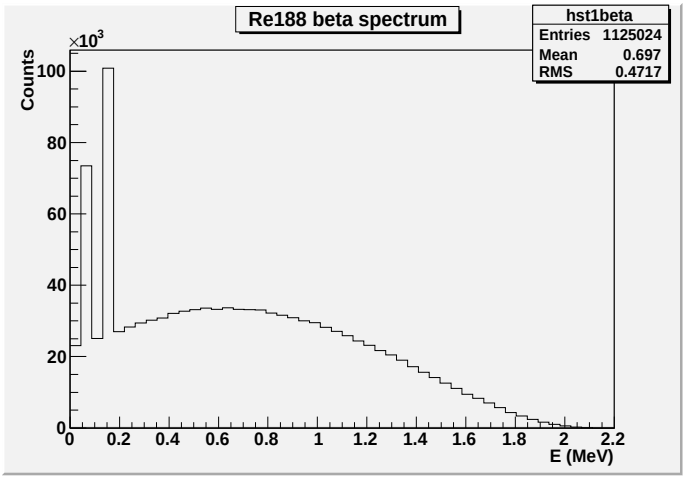

Figure 1.13:

^{188}Re β^- spectrum.

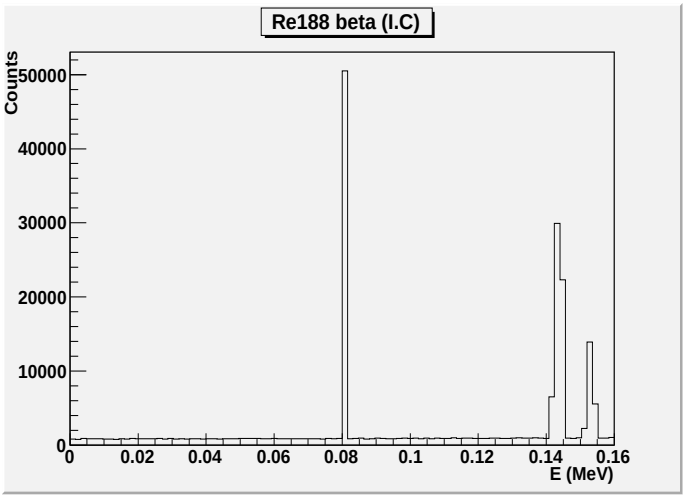

Figure 1.14:

^{188}Re internal conversion lines.

For the last check, to understand the effect of the medium surrounding the cells, we have first simulated two layers of cells at equal distance from the source, one close to a plexiglas layer and the other without it (Fig. 1.15a). The inner volume of the cylindric well is filled with a solution containing ^{188}Re (red color in the Fig. 1.15). The result of simulation is a much lower energy deposition (30% less) in the cell without the plexiglas layer. To restore the symmetry we added a plexiglas layer as show in Fig 1.15b. We have obtained respectively (297.8 ± 0.3) MeV and (298.3 ± 0.3) MeV for the top and bottom tissue layers.

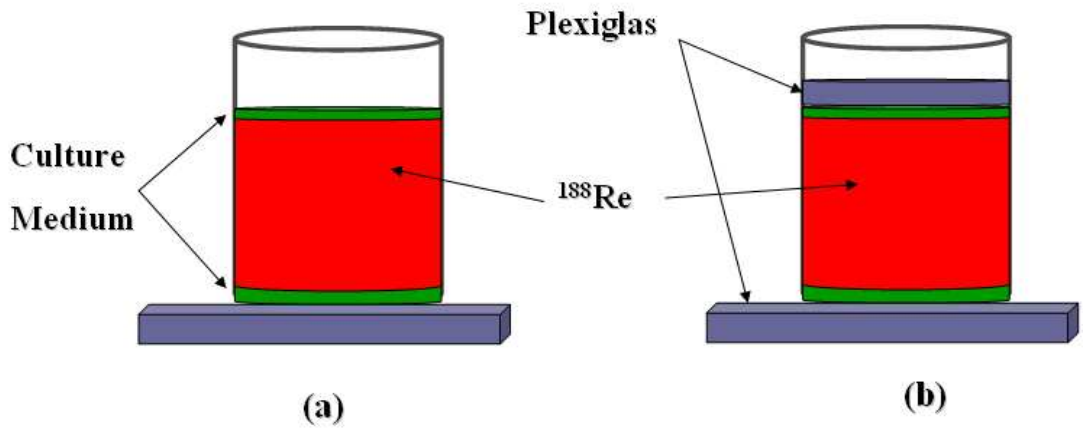

Figure 1.15: Third check of simulation setup.

We can conclude that all the results of the cross-checks show a good agreement with the expected values.

1.4.3 Results

To calculate the total dose absorbed by the cells, a computation of the average dose per ^{188}Re decay has been carried out using 10^6 simulated events. At this point, the dose corresponding to a given initial activity inside the active wells can be inferred by a simple rescaling.

Considering that the lifetime (τ) of ^{188}Re is 24.5 hours, and indicating with A_0 the initial activity, by using the formula:

$$A(t) = A_0 \cdot e^{-\frac{t}{\tau}} = \frac{dN}{dt} \tag{1.5}$$

we obtain that the total number of decays (N_{tot}) inside the solution containing ^{188}Re in 48 h (72 h) is:

$$N_{tot} = A_0 \cdot \int_0^{48h} \cdot e^{-\frac{t}{\tau}} = A_0 \cdot (1 - e^{-\frac{48h}{\tau}}) \tag{1.6}$$

An initial activity in the solution of 50μCi/cc corresponds about to 1.4×10^{11} Bq/cc (1.6×10^{11} Bq/cc) in 48h (72h). Being the volume of the radioactive solution contained within each well 0.23 cc, we obtain 3.2×10^{10} Bq (3.6×10^{10} Bq).

The GEANT4 simulation estimates an average energy deposition in the biological sample of about 280 eV per event. Therefore, the dose absorbed in 48 h (72 h) by each of the cell cultures deposited in the wells when the activity of the radioactive solution is 50 μCi/cc can be estimated as being approximately 6.3 Gy (6.9 Gy). Doses two and three times that large correspond, respectively, to the wells in the experimental setup filled with an initial activity of 100μCi/cc and 150μCi/cc.

It has been verified with the same GEANT4 simulation that, having the wells filled with the absorbing medium interleaved with the activated ones, it is possible to reduce the dose received from the nearby active cells to a negligible level. This is shown in Fig. 1.16 where the average dose deposited per event in the nearby wells, when only one of them is activated, is calculated using 10^8 simulated events.

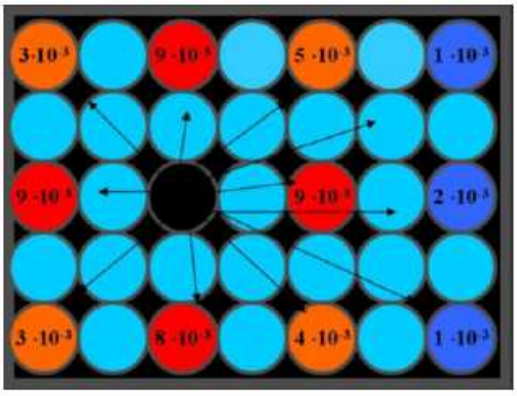

Figure 1.16: Average dose, in eV, deposited in the nearby cells when only one of them in the setup is activated.

Values below 10 meV, in nearby wells, are obtained with this setup, to be compared to the average energy deposition of 280 eV for a ^{188}Re decay inside the same well.

1.5 Experimental biodistribution

To study the effect of metabolic radiotherapy in small animals (mice), a small high-sensitivity γ-camera [32] has been built, following the experience of yttrium aluminum perovskite (YAP) camera [33][34] which is routinely used to image mice with ^{99m}Tc HA at the Laboratori Nazionali di Legnaro, Italy (e.g. [6]).

Figure 1.17 shows the experimental apparatus, as it is used in the laboratory. The γ-camera is based on a matrix of 66×66 Cerium doped YAP (YAP:Ce or $YAlO_3$:Ce) crystals [35], each measuring $0.6 \times 0.6 \times 10$ mm^3, with 5 μmm thick optical insulation between them. A Field Of View (FOV) of 40×40 mm^2 is thus achievable. The scintillator is read out by a R2486 Hamamatsu position sensitive photomultiplier [36],

with a 3 in. diameter photocathode. The anode consists of 16 plus 16 wires, crossing at 90° and connected by two resistive chains, defining the x and y directions. A 40 mm thick lead parallel hexagonal holes collimator [37], with hole diameter 1.5 and 0.18 mm septa, is placed in front of the YAP matrix. The detector is triggered using the last dynode and the ends of the x and y resistive chains. Its signals are amplified, stretched and read out by a NI 6023E card [38] connected to a Personal Computer (PC). All collected data are saved event by event in files stored on a hard disk for the offline analysis.

Figure 1.17: The experimental apparatus which is taking data at INFN in Legnaro (Padua - Italy). On the right one can see the mechanical structure and source positioning system, which contains the scintillator, the PM and the collimator inside the cylinder. The rack containing the readout electronics is visible on the left.

1.5.1 Energy resolution of the YAP camera

The energy response of the camera is calibrated as a function of the source position. For the calibration, a flat field of a solution containing ^{99m}Tc is taken, and the measured energies of the 140 keV photon are all equalized to the same value, everywhere in the FOV of the camera. The energy resolution (ER) of the setup, is thus determined by using a 6.8 mm diameter and 10 mm height plastic well filled with a solution with ∼0.3 GBq of ^{188}Re activity. This well is put under the YAP camera setup and data are acquired during 3 h. The total energy spectrum obtained from all the points originating from within the position of the well Region Of Interest (ROI) is shown in Fig. 1.18.

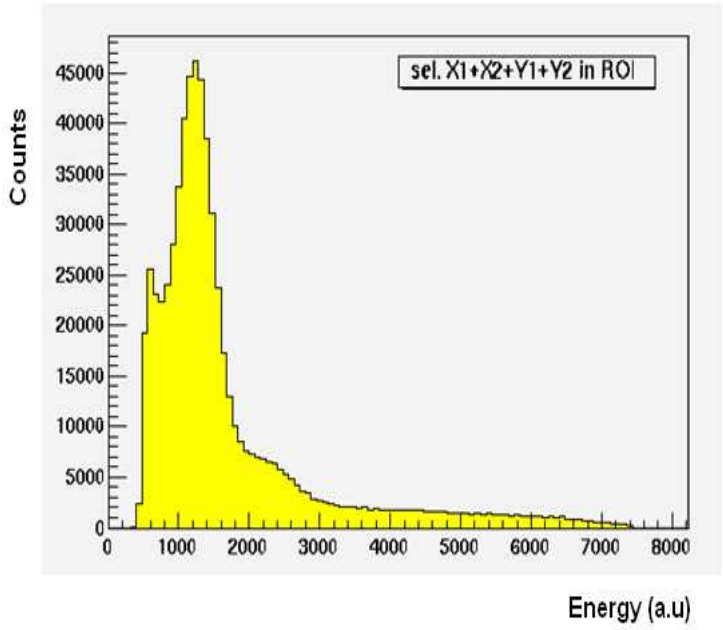

Figure 1.18: The total energy of a cylindrical ^{188}Re source measured in the YAP-camera. In the horizontal axis, the photon energy is expressed in arbitrary units, while in the vertical axis the corresponding counts are listed.

For the 155 keV ^{188}Re line, the energy resolution obtained in that way is 40% Full Width Half Maximum (FWHM).

1.5.2 Spatial resolution of the YAP camera

The digital-to-length conversion factor is determined using a set of three parallel capillaries, 0.7 mm wide and spaced 1.0 and 1.5 cm apart, filled with a solution of ^{99m}Tc. The image obtained from them is visible in Fig. 1.19. The Spatial Resolution (SR) obtainable in the present YAP camera setup with ^{188}Re, at 10 mm distance from the collimator is then determined by acquiring an image (as in Fig. 1.20) by using the same well described in Section 1.5.1. The SR is measured separately in the horizontal and in the vertical directions by deconvoluting a Gaussian shape from the known geometrical shape of the well in thin horizontal and vertical slices [39]. The results give a FWHM of (2.76 ± 0.10) mm in x and (2.72 ± 0.10) mm in y.

To increase the SR without losing sensitivity, and to obtain different projections simultaneously, we are building two new cameras to be positioned at 90° around a small animal. To obtain the biodistribution and tomographic information, they use as scintillators two planar crystals of $LaBr_3$:Ce, 50×50 mm^2 wide and 4 mm thick, read out by one H8500 Hamamatsu Flat panel PM each, with a glass window 3.0 mm thick protecting the crystal. The front-end electronics for the 64 channels of the H8500 has been designed using MPX-08 [40] chips. The system will be mounted on a rotating support, in order to produce tomographic images.

The different emission properties of ^{188}Re, compared to ^{99m}Tc, which emits just one single γ-ray at a fixed energy of 140 keV, imply a different design of the imaging camera. The higher image background is due to both β-rays and higher energies γ-rays interactions.

$LaBr_3$:Ce γ-cameras show superior SR and ER than the previous generation detec-

tors based on scintillation arrays of pixellated crystals [41].

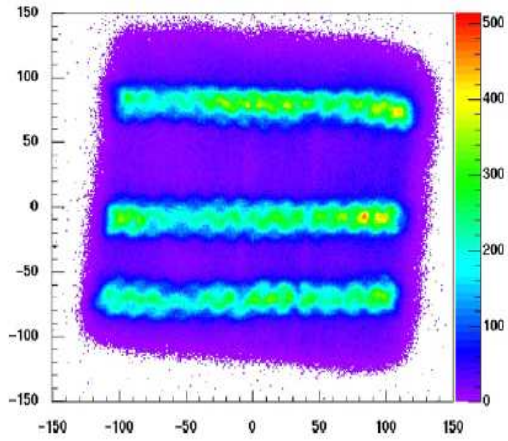

Figure 1.19: Image obtained with three capillaries filled with a solution containing ^{99m}Tc. (0.7 mm inner diameter, at a distance of 10 and 15 mm from each other)

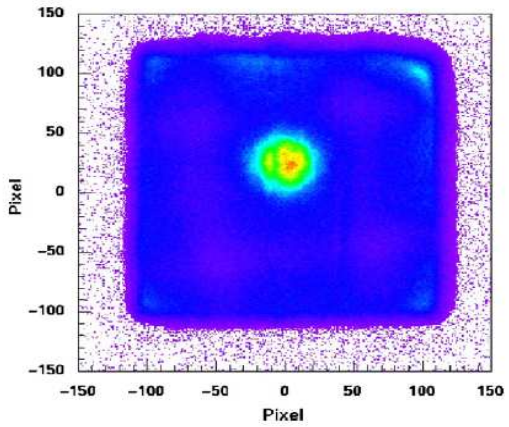

Figure 1.20: Image obtained with a plastic well of cylindrical shape, with a base diameter of 6.8 mm and a height of 10 mm, filled with a solution of ^{188}Re. The activity of the liquid is $\sim$ 0.3 GBq.

The better ER is expected to ease the separation of the 155 keV line of ^{188}Re with respect to the background photons produced in a large fraction of that isotope decay. Ongoing developments of the studies aimed at optimizing the imaging of ^{188}Re in vivo are presented in next Chapter, including the characterization of the PM and the scintillator.

1.5.3 First measurements with ^{188}Re

The labelling reaction of HA using ^{188}Re is carried out with good yields (65 - 70%) [42]. The radiolabelled compound was purified with a size exclusion chromatographic method before being used for biodistribution studies. Stability studies in rat serum confirmed the maintaining of the ^{188}Re linked to the polymer and there was no evidence of radio-decomposition after a few hours [42].

To test the full chain, from the radiolabelling to the imaging "in vivo", a C57 black mouse (healthy, female) has been injected with ^{188}Re-HA [4]. After general anesthesia, the solution with an activity of about 250 μCi is injected in the caudal vein. The mouse is positioned along the diagonal of the FOV, with the locus of injection outside it, and is monitored for about three hours. The image collected in the first five minutes shows a large spot close to the locus of injection in the tail (Fig. 1.21).

After 5 minutes, the activity concentrates roughly in the centre of the body, in a volume which contains the liver (Fig. 1.22). The activity is slowly decreasing during the 3 h of the measurement. After 3 h the mouse is sacrificed, and the organs are extracted and measured with a microcurimeter (Fig. 1.23). The liver contains 60% of the residual activity and close by organs another 20%, in agreement with the scintigrafic image (Fig. 1.22), where individual organs are not resolved.

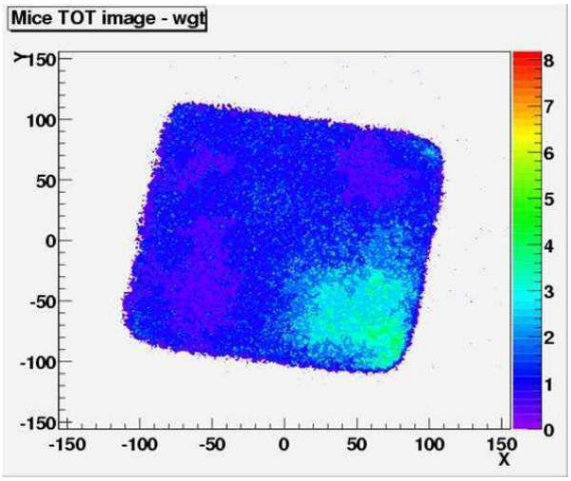

Figure 1.21: The image of the C57 mouse integrated for the first 5 minutes after the injection of ^{188}Re- HA in the caudal vein.

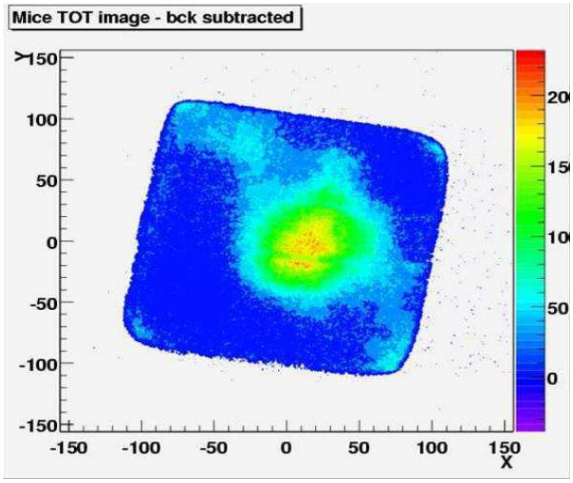

Figure 1.22: The image of the C57 mouse integrated between 5 and 185 minutes after the injection of ^{188}Re-HA in the caudal vein. The volume of large activity corresponds to the liver.

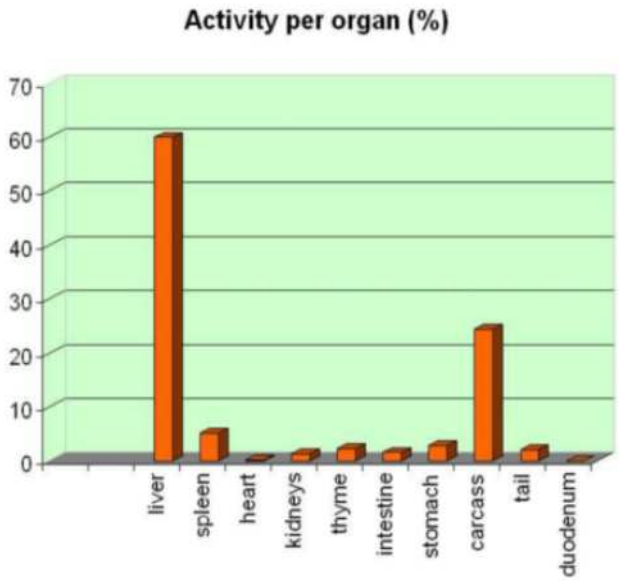

Figure 1.23: Activity of various organs "post mortem".

Even with limited resolution the test shows that it is possible to monitor the biodistribution of ^{188}Re in mice, with a potential saving in the number of animals needed for testing (as shown in Section 1.2.3) the ^{188}Re therapy.

Chapter 2

Lanthanum Bromide Crystals

2.1 Introduction

Over the last few years scintillation crystal machining has greatly improved. At the same time new scintillating crystals suitable for Medical Imaging have appeared on the market. It is possible to built Sodium Iodide doped with Thallium (NaI:Tl) arrays with about 1.0 - 1.1 mm pixel size and good light output, or Cesium Iodide doped with Thallium (CsI:Tl) scintillation arrays with sub-millimeter pixel size. The main limitation offered by scintillation arrays is the SR as limited by pixel size and the ER response limited by dead zones between crystals pixels. In continuous and pixellated crystals, the scintillation event position is usually calculated by the Anger algorithm [43], which determines the location of each scintillation event, as it occurs, using the weighted average of signals coming from the photodetectors that operate the sampling of the scintillation light distribution. The possible limitation to the use of continuous crystal is the bad linearity (L) response, and as a consequence the poor SR, which arises in small FOV gamma cameras assembled with planar crystals [44].

A $LaBr_3$:Ce scintillation crystal cannot be machined in small pixel size, since it

is fragile. It has a light yield (LY) almost twice higher than NaI:Tl (see Table 2.2) and it has very similar absorption radiation properties and refraction index as NaI:Tl (see Table 2.1). To understand better the potentials of this scintillation crystal in gamma ray imaging, a more complete study of different continuous $LaBr_3$:Ce crystals, performed by GEANT4 simulations, is described in the following. In particular the work is focused on the scintillation light distribution and how they affect L.

2.2 Lanthanum Bromide features

The scintillation properties of $LaBr_3$ doped with 0.5% Ce_3+ have been presented for the first time in 2001 by Delft and Bern Universities. The peculiar features of $LaBr_3$:Ce, vs other crystals, are shown in Tab.2.1 and 2.2 (see also [45]).

In Fig. 2.1 the absorption curves are shown as a function of $LaBr_3$:Ce crystal thickness and of γ-photon energies. Intrinsic efficiency (@ 140 keV) is 80% and 70% respectively for 5 mm and for 4 mm thick crystals. The ^{137}Cs spectrum, published by Saint Gobain [46], shows ER of 3% at 662 keV (Fig. 2.2).

Table 2.1: $LaBr_3$:Ce and NaI:Tl properties: attenuation @ 140 KeV

	Decay Time (ns)	Att. Len. (mm)	λ Max (nm)
$Labr_3$:Ce	16 (97%)	3.6	380
NaI:Tl	230	4.9	410
BGO	300	0.8	480
CsI:Tl	1000	2.4	550
LSO	40	1.0	480

Table 2.2: $LaBr_3$:Ce and NaI:Tl properties, refractive @ λ Max

	Density (g/cm^3)	LY (ph/MeV)	Refractive Index
$LaBr_3$:Ce	5.3	63000	1.90
NaI:Tl	3.7	38000	1.85
BGO	7.1	9000	2.15
CsI:Tl	4.5	52000	1.79
LSO	7.4	28500	1.82

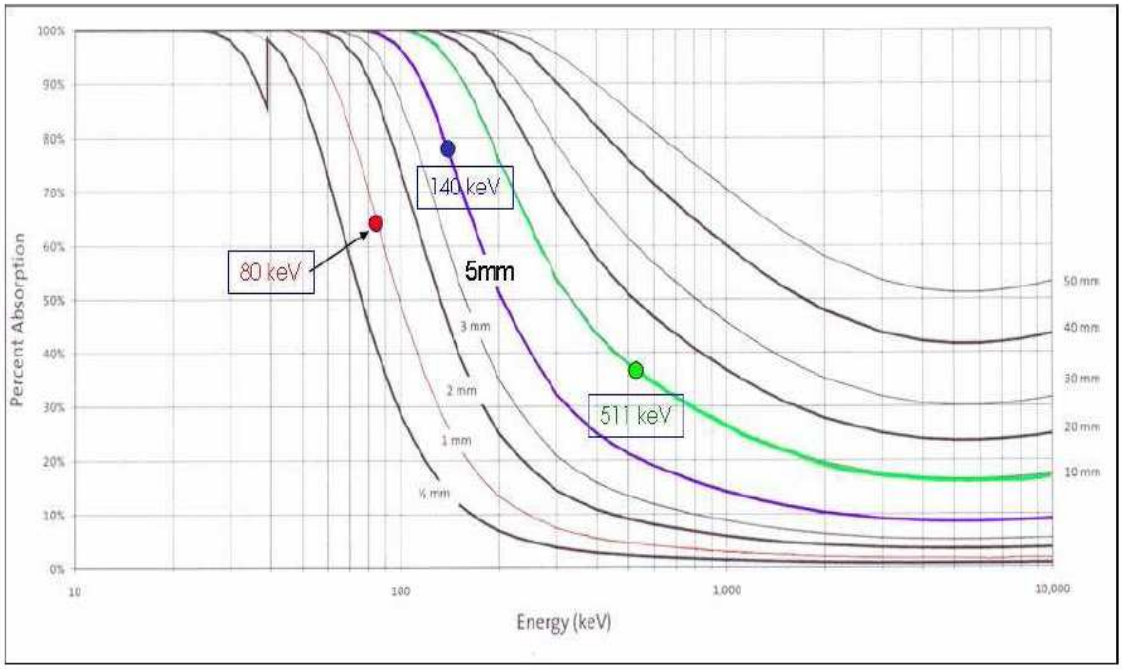

Figure 2.1: Absorption curves (%) in a $LaBr_3$:Ce as a function of gamma-ray energy and crystal thickness.

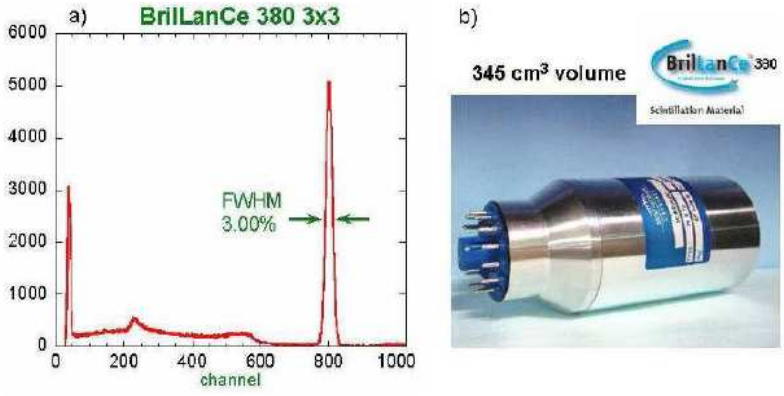

Figure 2.2: ^{60}Co spectrum (Saint Gobain) measured with a $LaBr_3$:Ce crystal.

2.3 Experimental setup

Preliminary tests are performed on a crystal ($48 \times 48 \times 4$ mm^3). The crystal (Fig. 2.3) is covered on the front and lateral side with an aluminium case (0.5 mm thick), while on the back side it is coupled to a single Flat Panel Position Sensitive PM through an optical glass window 3 mm thick.

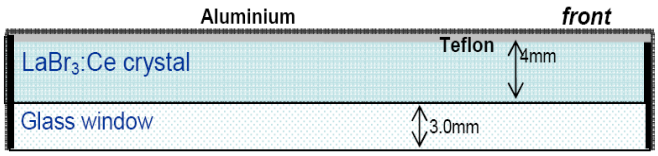

Figure 2.3: Side view of the $LaBr_3$:Ce planar crystal assembly.

The front surface is covered with white diffusive reflector (Teflon 0.3 mm thick) in order to reflect the light output emitted opposite to the PM and increase the light

output. A black light absorber is placed on the lateral surfaces of the crystal and of the glass proctecting the crystal (CG) lateral surfaces to avoid light reflections which will cause Point Spread Function (PSF) distortions. The Hamamatsu H8500 Flat Panel PM [36] has an external size of 52 × 52 × 27.4 mm^3. A bialkali photocathode and 12 stages metal channel dynode are used as electron multiplier. A 8×8 matrix anode (64 channels), with pixel size of 5.8 × 5.8 mm^2, is used for a position sensitive function in which each individual pixel has a 6.08 mm pitch. The overall active area is 49.0 mm squared. The PM is characterized by a glass window thickness (PMG) of 1.5 mm, an anode dark current of 1 nA and by an anode gain variation range of about 45:100. The PM gain is about $1.5 \cdot 10^6$ at -1100V and the quantum efficiency (QE) of the PM is 27% at the peak of the emission spectrum of $LaBr_3$:Ce, according to the manifacturer's design specifications (see Fig. 2.4).

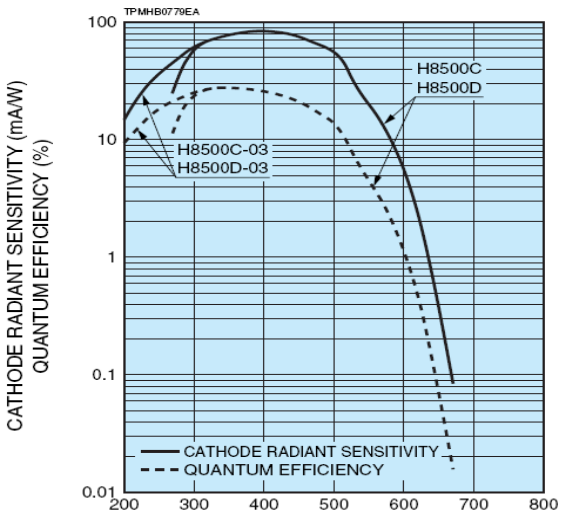

Figure 2.4: H8500 series: QE vs emission lenght.

2.4 Photodetection principle

The 8×8 anodic array of the H8500 (MA-PMT) is shown schematically in Fig. 2.5, where n_j^k represents the charge signal readout on the k-th row and j-th column of the anodic array. SR depends on the the statistical uncertainty of the scintillation position measurement. Such a position is determined by using the MA-PMT and a centroid algorithm ("linear") elaborated by Anger in 1958 that it is, still now, the basic principle of imaging reconstruction in modern scintillation gamma cameras [43]. The centroid algorithm calculates the position (X,Y) of the scintillation event by the average values of the measured charge distributions, which represents a point in the imaging plane. Many γ-ray interactions then give rise to the image of the emitting source.

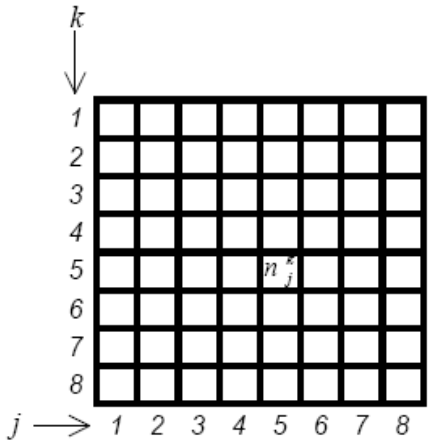

Figure 2.5: Schematic drawing of the anodic structure of the H8500.

The "linear" algorithm applied on a charge distribution can be written as follows:

$$X_C = \frac{\sum_j n_j x_j}{\sum_j n_j} \tag{2.1}$$

where $n_j = \sum_k n_j^k$ is the "projection" of the charge collected along the j-th column, x_j is the anode coordinate and X_c is the centroid coordinate along the x-direction. The same applies along the y direction:

$$Y_C = \frac{\sum_k n_k y_k}{\sum_k n_k} \tag{2.2}$$

here $n_k = \sum_j n_j^k$ is the "projection" of the charge collected along the k-th row, y_k is the anode coordinate and Y_c is the centroid coordinate along the y-direction.

SR relates to the ability of the imaging system to distinguish between two closely spaced objects on an image; in particular SR is the minimum distance between two point sources that are reproduced as distinct by the detection system and it is related to the statistic uncertainty of the scintillation event position $\sigma^2_{X_C}$ ($\sigma^2_{Y_C}$) of the X_c (Y_c) coordinate of the scintillation event. By applying the statistical definition of standard deviation $\sigma^2_{X_C}$ ($\sigma^2_{Y_C}$) we can write:

$$\sigma_{X_C} = \frac{\sigma_{charge}}{\sqrt{n_{phe}}} \tag{2.3}$$

Where σ_{charge} represents the standard deviation of the charge distribution as projected along x direction (y direction for σ_{Y_C}), and n_{phe} the average number of photoelectrons. So the SR of the detector measured as FWHM, is:

$$SR = FWHM_{PSF_{image}} = \frac{FWHM_{cd}}{\sqrt{n_{phe}}} \tag{2.4}$$

where $FWHM_{cd} = 2.35 \cdot \sigma_{charge}$ is the full width at half maximum of the projected charge distribution.

A "quadratic" algorithm [47] has been used applying a squaring procedure to the charge distribution collected from MA-PMT. The "linear" algorithm is modified by the following:

$$X_C = \frac{\sum_j n'_j x_j}{\sum_j n'_j} \tag{2.5}$$

with

$$n'_j = \sum_k (n_j^k)^2 \tag{2.6}$$

Experimental values are influenced by a light background into the crystal, which affect σ_{charge} and consequently also SR. For all reconstruction algorithms, it is possible to set a threshold (t) useful to remove the light background. Eq. 2.6 becomes:

$$n''_j = \sum_k (n_j^k - t)^2 \tag{2.7}$$

and the "quadratic" algorithm:

$$X_C = \frac{\sum_j n''_j x_j}{\sum_j n''_j} \tag{2.8}$$

In Fig. 2.6, we show the PSF of light (PSF_{light}) coming from an ideal (without fluctuations) scintillation event and the image (PSF_{image}) obtained from many scintillation events.

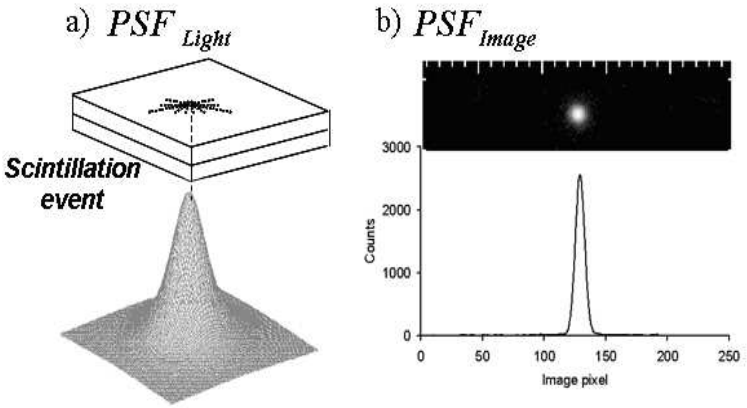

Figure 2.6: The PSF of an ideal scintillation event (left) and a PSF image as due to the many scintillation (right).

In Fig. 2.7 is shown the reconstruction technique from an ideal scintillation event made of three principal steps needed to obtain the X and Y position of each scintillation

event. In in Fig. 2.7a. the light scintillation spread. In Fig. 2.7b the MA-PMT operates a sampling of the PSF_{light} obtaining the charge distribution shown. In Fig. 2.7c the charge projection along one direction.

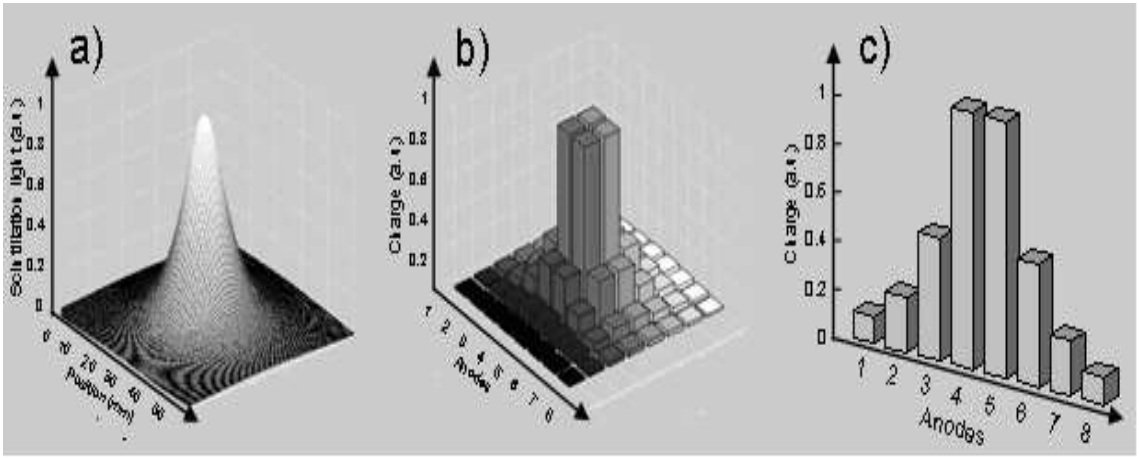

Figure 2.7: Reconstruction technique from an ideal scintillation event a) Light scintillation spread. b) Charge distribution as sampled by the anode array. c) Charge projection along one direction, ready to apply the centroid algorithm.

2.4.1 Linearity and Spatial Resolution

L relates to the ability of an imaging device to reproduce linearly the displacements of a radioactive source across the face of the detector. It can be visualized by plotting real (or mechanical) position versus measured position (Fig. 2.8).

L is defined as:

$$L = \frac{\Delta X_{measured}}{\Delta X_{mechanical}} \tag{2.9}$$

which represents the angular coefficient of L curve at each measured point. L is then useful to describe the deviation from a perfectly linear behaviour (L=1) and represents

a calibration to convert distances reproduced in the image to the "real" distances of the object [48].

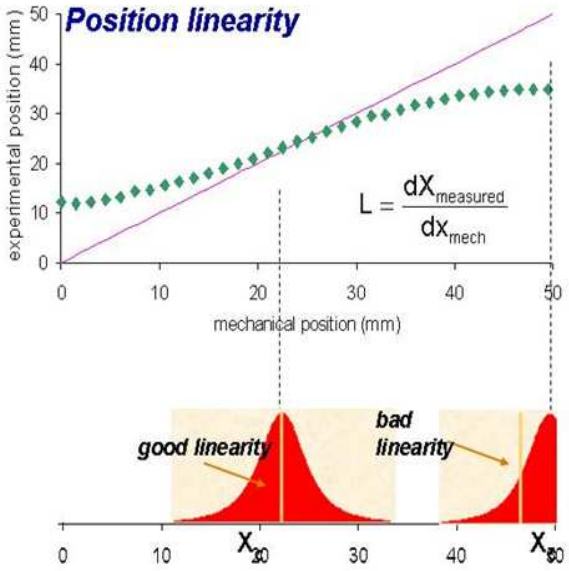

Figure 2.8: Light edge effect.

In the Anger Camera, L is affected by the edge effect, since when gamma-rays interacts at a point in the crystal near the boundary, the charge distribution shape is altered and the mean position estimated by the centroid algorithm is no more equal to the maximum of the light distribution (Fig. 2.8). A good L means then that the centroid algorithm reproduces correctly the real (mechanical) position. A bad L causes image compression and worsen the SR. In fact, assuming a poissonian distribution for n_j^k, we define SR by:

$$SR = \frac{1}{L} \cdot \frac{FWHM_{cd}}{\sqrt{n_{phe}}} \tag{2.10}$$

In Section 2.6 we will calculate FWHM of the charge spread distribution, L and SR by applying "linear" and "quadratic" algorithms on a photoelectrons distribution,

using simulated and experimental data.

2.4.2 Energy Resolution

The ER is defined as the full width (ΔE) of the peak in the pulse height spectrum at half the maximum intensity, divided by the central energy value:

$$ER = \frac{\Delta E}{E} \tag{2.11}$$

ER is an important parameter for imaging devices since image contrast mainly relates to the ability of the detector of discriminating between photopeak events and Compton-diffused photons. When spectrometry measurements are performed with scintillators optically coupled to photomultiplier tubes, ER is proportional to the standard deviation of the charge that reaches the anode in each scintillation event. Charge production consists of five sequential processes each dependent on the previous one that can be described as follows:

- Production of scintillation photons in the crystal due to gamma-ray interaction;
- Collection of scintillation photons at the PM photocathode;
- Production of photoelectrons in the photocathode due to incident scintillation photons;
- Collection of photoelectrons at the first dynode in the PM;
- Multiplication of electrons by the dynodic chain.

ER can be parameterized [49][50] as:

$$ER = \sqrt{(ER_{sta})^2 + (ER_{int})^2} \tag{2.12}$$

where ER_{int} is an additional intrinsic resolution which has been interpolated from experimental data in [50] for $LaBr_3$:Ce and yields $(4.5 \pm 0.5)\%$ for 140 keV photons. ER_{sta} represents the Poissonian component of ER given by the square root of the number of collected photoelectrons. The variance of the electron multiplier gain [50] is not taken into account in the calculation of the total energy resolution.

The intrinsic component of ER was first observed in 1956 (Kelly et al.). Since then onwards a lot of studies [51][52], recently [53], have investigated the origin of this non poissonian contribution which still represents the main limitation to the overall ER. The exact mechanism has not been fully explained yet, nevertheless some conclusions are to date widely accepted :

- differences in light production at different crystal locations, probably due to crystal lattice defects;
- crystal growth methods used by the manufacturer for production of "large crystal size".

In addition to the intrinsic energy resolution, the scintillation light yield is affected by a non proportionality of the emitted light with energy of gamma ray released to the crystal. This effect is main related to the type of interaction.

2.5 Simulation setup

For the modeling of the electromagnetic interactions, the "Penelope" [54] model available with GEANT4 (4.9.0 version) is used. Atomic relaxations following photoelectric effect, Compton scattering, ionization interactions, Rayleigh scattering, fluorescence photons and Auger electrons are simulated. GEANT4 allows also the transport and boundary effects for the optical photons (see appendix A) generated by the scintillat-

ing crystal to be simulated. Figure 2.9 shows the simulated set up by GEANT4. The simulated scintillation camera reproduces the geometry of the experimental setup (see Section 2.3). The CG and PMG, respectively 3.0 mm and 1.5 mm, are composed of the same glass material (same optical proprieties). Initially, to emulate the black light absorber wrapping the experimental crystal and the CG, the *reflectivity* (R) of the lateral surface of the simulated crystal has been set equal to zero. As explained in the following (see Section 2.6), it is found, comparing with the experimental data, that a certain amount of light is reflected in fact, and a different value of R is used for the final simulation setup.

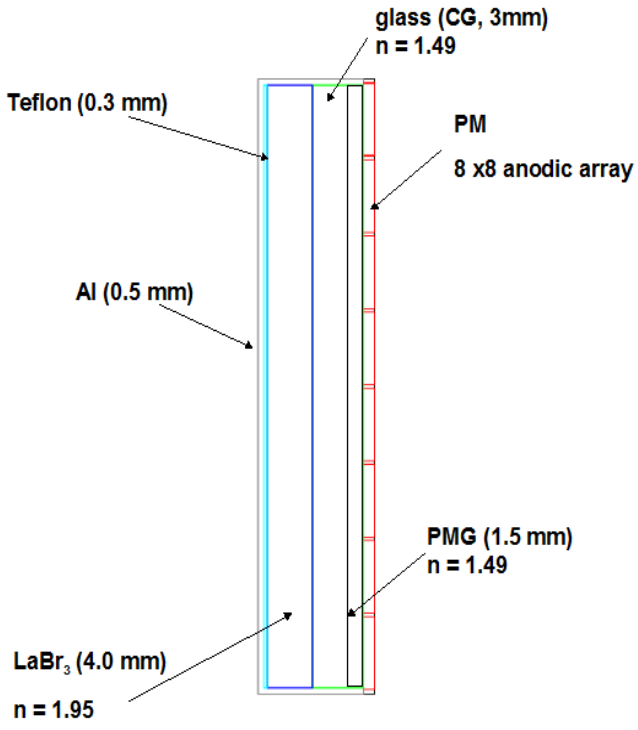

Figure 2.9: The set up used in the simulation.

The MA-PMT is emulated by reading out in the simulation output the number of

photons reaching the readout surface in a grid of 8×8 squares. The QE of the PM is emulated by setting the surface between PMG and PM (active area) as $dielectric - metal$ with an $efficiency$ of 0.27. In the simulation, the boundary processes of all crystal surfaces follow the rules of the UNIFIED model, developed for the DETECT project [55]. The optical properties of the materials involved in the simulations (refractive index, absorption and scattering lengths) are gathered from literature [56]. A scintillation light yield equal to 63000 photons/MeV is assumed for $LaBr_3$:Ce. The scintillation photons are generated as a pure Poisson process ($resolutionscale = 1$, see Appendix A). In Fig. 2.10 we show the scintillation photons produced by an interaction of an 140 keV energy photon into a $LaBr_3$:Ce crystal [1].

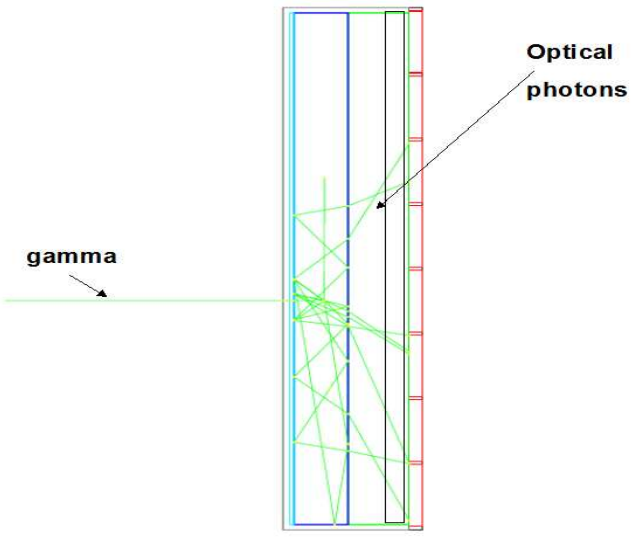

Figure 2.10: The set up used in the simulation including a sketch of optical photons.

In the UNIFIED model some combinations of surface properties, such as Polished

[1]For a correct and clear visualization of the optical photons, a scintillation light yield equal to 60 photons/MeV is assumed to get this image.

or Ground, enumerate the different situations which can be simulated. In all cases, the surfaces are made up of micro facets with normal vectors that follow a given distribution (see Fig. 2.11). The angle between a micro-facet normal and the average surface normal, α, is assumed to follow a gaussian distribution of standard deviation σ_α and n_1, n_2 are respectively the indexes of refraction of the incident and transmission medium.

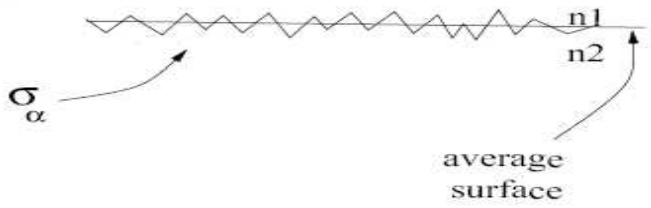

Figure 2.11: Micro-facets and average surface.

The Polished model is meant to account for a perfectly polished surface. Photons incident on the surface are assumed to have random polarization, and are first tested for the possibility of Fresnel reflection if a change in refractive index occurs at the surface. If reflection does not occur, the optical photon is transmitted with the complementary probability given by:

$$T = 1 - R \tag{2.13}$$

If reflection occurs, the angle of reflection is set equal to the angle of incidence (Fig. 2.12 on the left).

The Ground option is available to simulate a rough or ground optical surface. It is treated in the same way as the polished surface described above, except that the reflection (refraction) follows a Lambertian distribution. (Fig. 2.12 on the right).

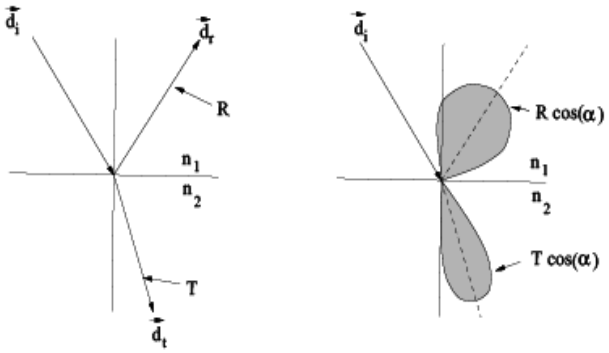

Figure 2.12: Modelization of the reflection on the surface of the scintillating crystal: Polished (left) and Ground (right).

In the simulation to emulate a completely white diffusive experimental surface, the $LaBr_3$:Ce front surface has these (optical) parameters:

- $dielectric - metal$;
- ground;
- R = 0.95;
- $\sigma_\alpha = 0.0$;
- $C_{dl} = 1$;
- $C_{sl} = C_{ss} = C_{bs} = 0$;

where C_{dl} is the diffuse lobe constant for the probability of internal Lambertian and reflection, C_{sl} is the specular lobe constant that represents the reflection probability

about the normal of a micro facet, the C_{ss} is the specular spike constant illustrates the probability of reflection about the average surface normal and finally C_{bs} is the back-scatter spike constant for the case of several reflections within a deep groove with the ultimate result of exact back-scattering.

We apply the Snell's Law for the surface between crystal and CG. For the lateral surfaces of the PMG we set R = 0.0 [2].

For more details about the simulation of optical photons, see Appendix A.

2.6 Results

First of all, using GEANT4 we have simulated a pencil beam of 140 keV photons[3] impinging the crystal (at the centre), and we have calculated the average depth of interaction within the $LaBr_3$:Ce crystal (located at about 2.33 mm from the crystal back surface as shown in Fig. 2.13).

The gamma generates some optical photons as shown in Fig. 2.10. Some of them travel directly through the CG and PMG windows towards the PM. Some others are reflected by the lateral surfaces or by the front side of the crystal. In this first test, all the surfaces of the setup are supposed complectly black (total absorption of the optical photons, using R = 0). The fraction of optical photons (starting from the interaction point) moving towards the CG resulted to be $(44.9 \pm 0.4)\%$ in the simulation. In the theoretical expectation, based on purely geometric arguments (see Fig. 2.13), considering the angle $\theta_{cry} = arctg(\frac{24.0}{2.33})$, it is possible to obtain the fraction of optical

[2]When R = 0.0, it is not necessary to specify all other optical proprieties.

[3]The energy of the γ-ray produced in the ^{99m}Tc decay. This energy value is the same used for the experimental measurements. We have used 10^4 photons

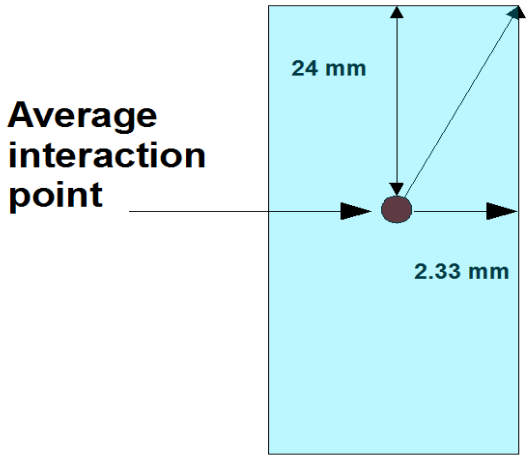

Figure 2.13: Simulated average interaction point in the $LaBr_3$:Ce crystal.

(f_{opt}) using the formula:

$$f_{opt}(\%) = 100.0 \cdot \frac{\Delta\Omega}{4\pi} \tag{2.14}$$

where $\Delta\Omega$ is given by:

$$\Delta\Omega = 2.0 \cdot \int_0^{\theta_{cry}} \int_0^{2\pi} sin(\theta) d\theta d\varphi \tag{2.15}$$

Considering the limit angle given by:

$$\theta_{lim} = arcsin(\frac{n_{glass}}{n_{cry}}) \tag{2.16}$$

the expected fraction of optical photons moving towards the PM is 19.0%, to be compared with an MC value of $(18.8 \pm 0.2)\%$.

As we have seen in Section 2.4, by MC it is possible to show the effects on the charge distribution using "linear" or "quadratic" algorithms with or without threshold level. Figure. 2.14 and Fig. 2.15 show respectively the charge distribution spread for a single gamma central and lateral interaction. In particulary, Fig. 2.14b and 2.15b show the effect of a threshold level (5% of the maximum) on the charge distribution

and in Fig. 2.14c and Fig. 2.15c the squared charge distribution (with threshold) are shown.

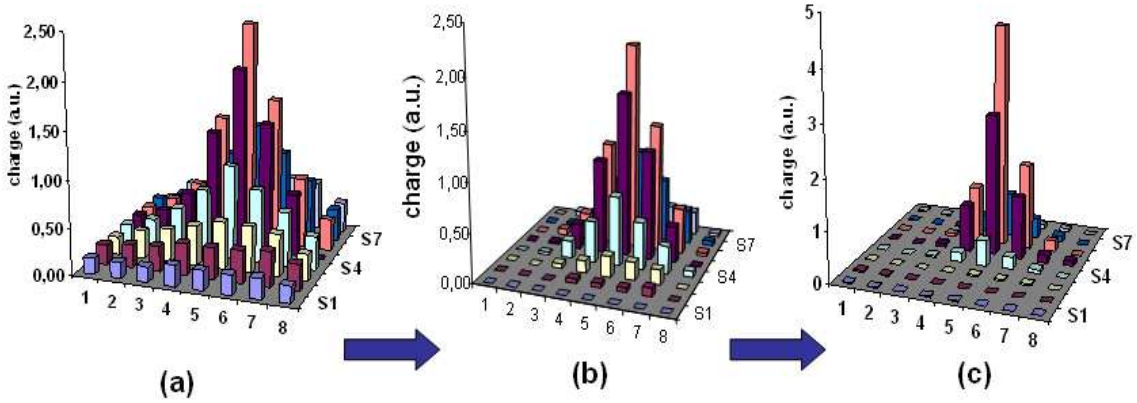

Figure 2.14: Simulated charge distributions (central interaction).

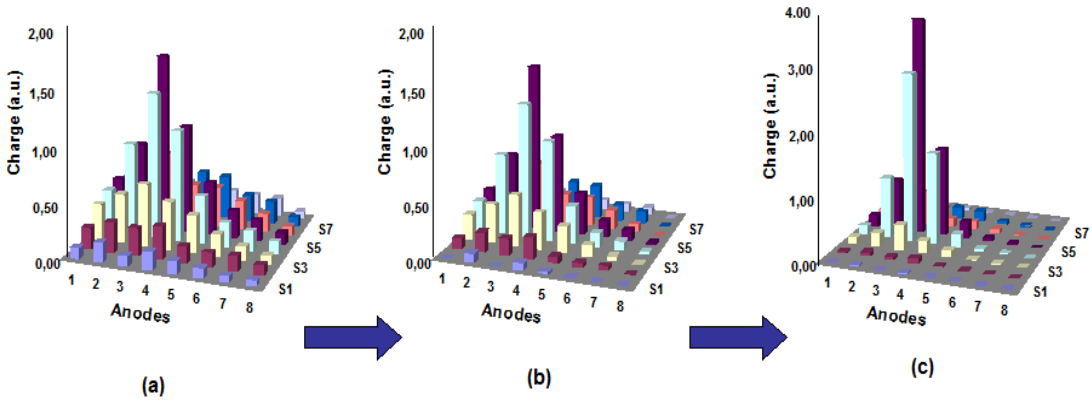

Figure 2.15: Simulated charge distributions (lateral interaction).

The better reconstruction of interaction point by "quadratic" algorithm (with a threshold) is clearly evident mainly for a lateral interaction (in the Fig. 2.15c with

respect to Fig. 2.15a).

In the second test, we have calculated (Figure 2.16) the number of detected optical photons in correspondence of different R values of the crystal and CG lateral surfaces, using $dielectric - metal$ and the polished model[4]. Photons interact at the centre and at the border of the crystal. In our experimental setup, the light collected when the source is near the edges is about $80 - 85\%$ of that collected when the source is at the center. This experimental result can be possible only if the considered lateral walls are not perfectly black. In fact, in case of total absorption, one should expect instead that the light collected when the source is located near the edges of the crystal is roughly half of that collected when the source is at the center of the crystal (as visible in Fig. 2.16).

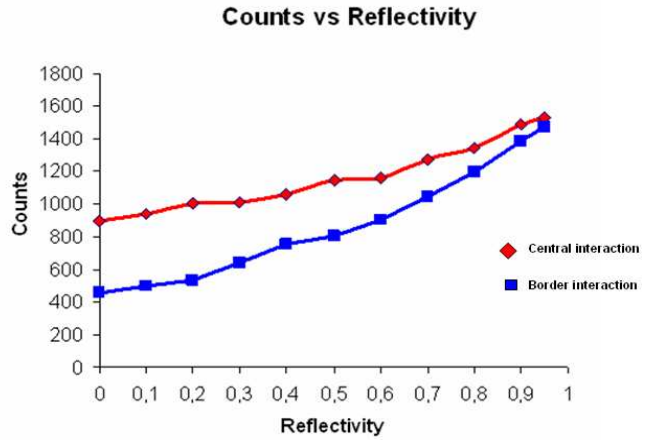

Figure 2.16: Number of detected photons with the gamma impinging at the centre and at the border of the crystal, as a function of the reflectivity of the crystal and CG lateral surfaces.

Considering the optical parameters just set in the simulation setup, described in Section 2.5, we found a (preliminary) agreement between experimental and simulated

[4]In this case: $C_{ss} = 1$ and $C_{sl} = C_{dl} = C_{bs} = 0$

data using (for the crystal and CG surfaces next to aluminum wrapping):

- $dielectric - metal$
- Polished model;
- $\sigma_\alpha = 0.0$[5]
- R = 0.6;

As a consequence of the preliminary results, we have to assume that the considered lateral surfaces are indeed not perfectly black, and they could reflect back some amount of light. To verify this statement, we have decided to use a comparison with the experimental data by using the sigma (σ_{pcd}) [47] of the projection (on one of two read out coordinates) of the collected charge distribution, event by event. We have simulated the $LaBr_3$:Ce crystal (and CG) with lateral walls reflection coefficients varying from 0.5 to 0.8. The results obtained are shown in Fig. 2.17 where the sigma values of the simulations, done with $R = 0.5$, 0.6, 0.7 and 0.8, are compared with the experimental data.

These sigma values are evaluated from the charge distributions obtained using a pencil beam impinging both at the center and at the border of the crystal. For every step of R, $4 \cdot 10^4$ photons of 140 keV are used[6]. We observe again that the experimental and simulated data agree well, with one another, for a value of $R = 0.6$ (see also Fig. 2.18).

We can conclude that the crystal and the CG used for our experimental measurements has not the ideal optical properties we expected, but we can suppose instead that the lateral surfaces reflect scintillation light back into the crystal.

[5]We have supposed that polished surface are perfect.

[6]Optical photons simulations need a lot of CPU time.

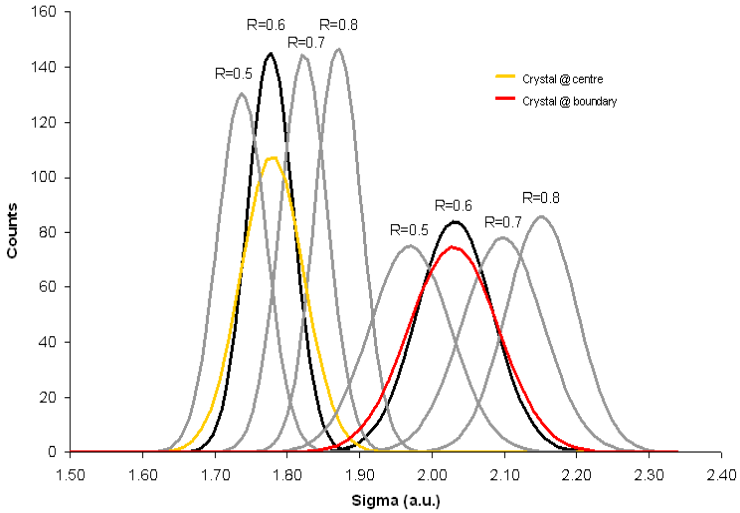

Figure 2.17: σ_{pcd} comparison for simulated and experimental data at the center and at the boundary of the crystal. The simulation is performed with different reflectivity values.

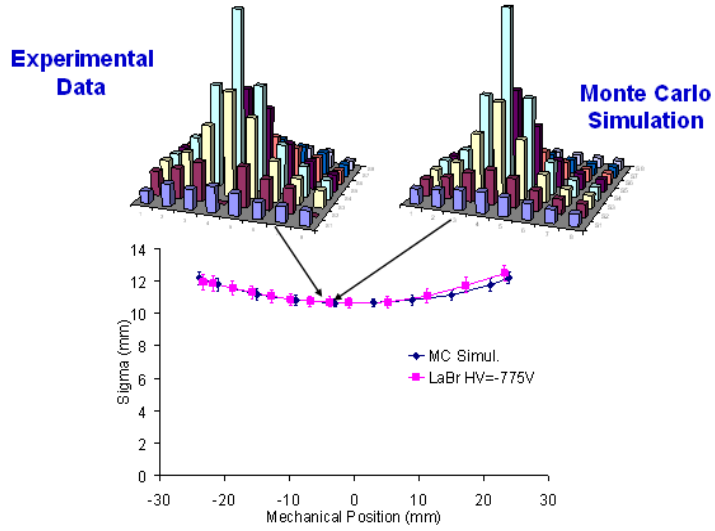

Figure 2.18: Monte Carlo (Polished model, R = 0.6) vs experimental data: charge distribuition spread @ 140 keV.

To study other possible crystal configurations, in view of looking for the most performant gamma camera based on $LaBr_3$:Ce crystals, three different crystal assembly are simulated: "Ground", "Polished" and "Air Gap". "Ground" and "Polished" refer to the status of the lateral surfaces of the crystal and of the CG, as already discussed, while "Air Gap" is the "Ground" model with a thin air interface (0.1 mm) between the CG and the PMG. For every model, the front surface is the same just described in Section 2.5. For the "Ground" model, we have used for crystal and CG lateral surfaces:

- $dielectric - metal$ and ground model;
- $\sigma_\alpha = 0.0$;
- $C_{dl} = 1$ and $C_{sl} = C_{ss} = C_{bs} = 0.$;

Figures 2.19 2.20 and 2.21 show the energy spectra obtained by a central interaction in the crystal, respectively for "Polished", "Ground" and "Air Gap" model, with superimposed a gaussian fit.

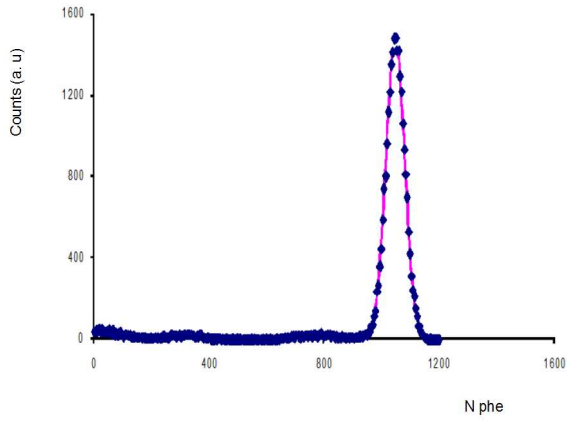

Figure 2.19: "Polished" model: energy spectrum with superimposed a gaussian fit (continuous line).

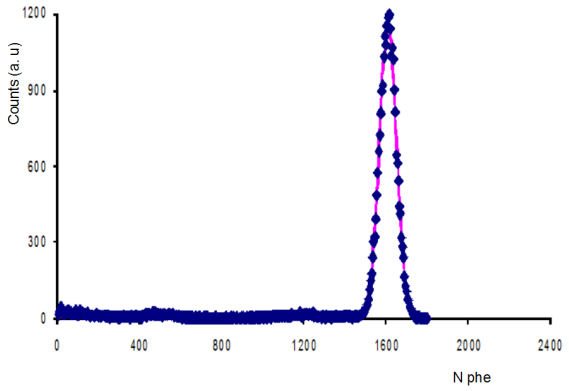

Figure 2.20: "Ground" model: energy spectrum with superimposed a gaussian fit (continuous line).

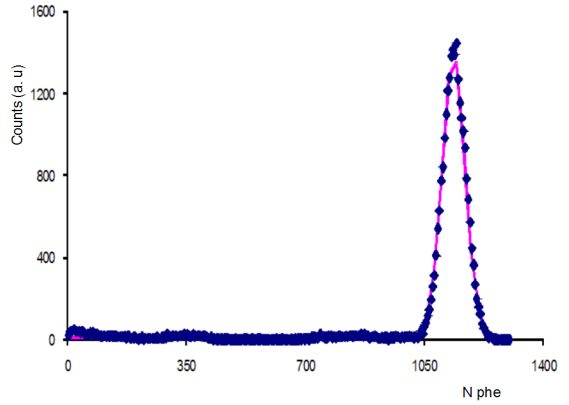

Figure 2.21: "Air Gap" model: energy spectrum with superimposed a gaussian fit (continuous line).

The crystal is scanned using a pencil beam impinging different positions with 2 mm step. For every step, $2 \cdot 10^4$ photons of 140 keV are used. Figures[7] 2.22, 2.23 and 2.24 show the profiles of the scanning performed by "linear" (left) and the "quadratic"

[7]One pixel is equal to 0.085 mm for a 512 $\times$ 512 digitization.

(right) algorithms, respectively for "Polished", "Ground" and "Air Gap" models. The better "visibility" of the profiles, obtained by weighting the central anode position with the quadratic algorithm (right) is evident.

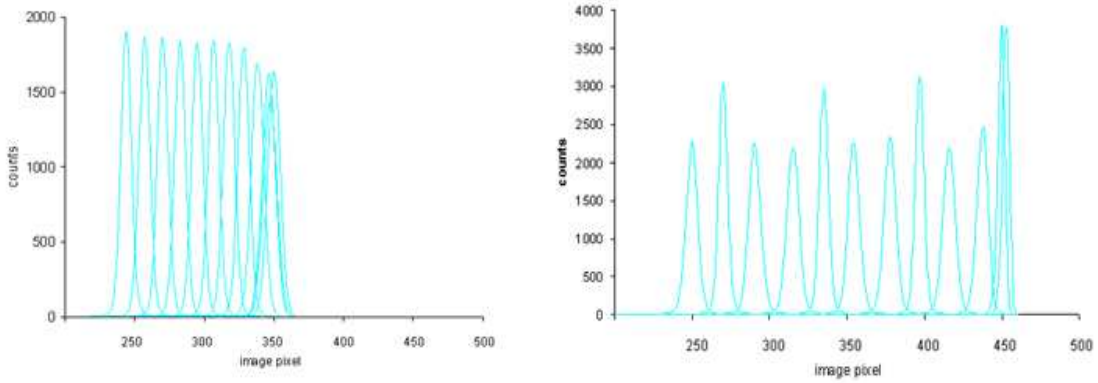

Figure 2.22: "Polished" model: the profiles of the scansion performed with a pencil beam impinging different positions with 2 mm step, using "linear" (left) and the "quadratic" (right) algorithms.

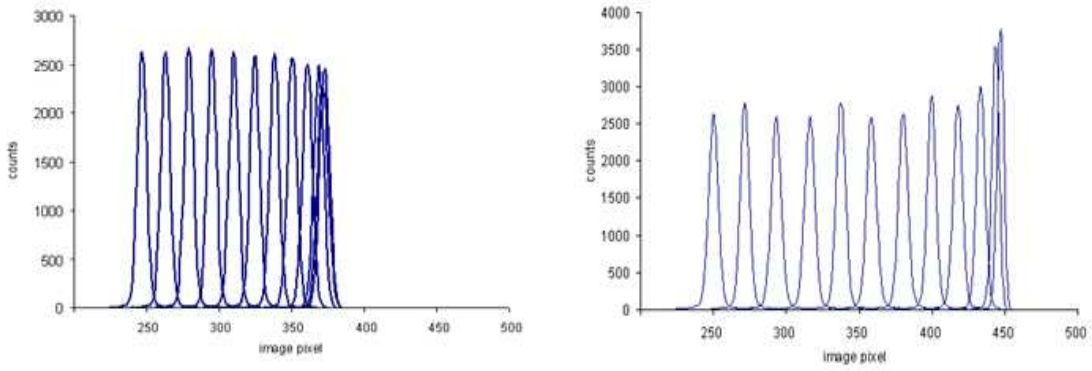

Figure 2.23: "Ground" model: the profiles of the scansion performed with a pencil beam impinging different positions with 2 mm step, using "linear" (left) and the "quadratic" (right) algorithms.

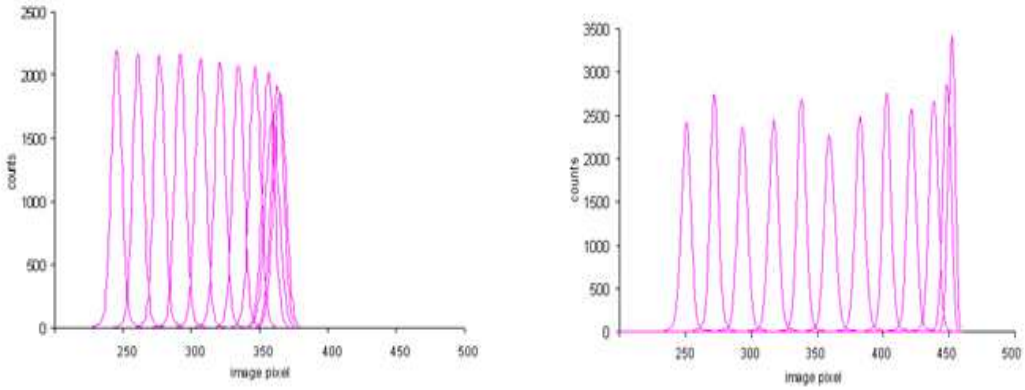

Figure 2.24: "Air Gap" model: the profiles of the scansion performed with a pencil beam impinging different positions with 2 mm step, using "linear" (left) and the "quadratic" (right) algorithms.

Experimentally, the crystal is scanned with 0.4 mm collimated ^{99m}Tc spot source with 2 mm step. Fig. 2.25 compares the determination of the position as obtained, in the three optical models, with the "linear" and the "quadratic" algorithms. The better L value obtained by weighting the central anode position with the "quadratic" algorithm is clear, even if the non-linearity at the edges is still present. The SR analysis, comparing MC and experimental data, is shown in Fig. 2.26 that shows three different interaction points (step 2 mm) at the centre of the crystal.

Finally, the ER values, the average number of photoelectrons gained by anode, SR and L are respectively summarized in Table 2.3, Table 2.4 and Table 2.5. The statistical values (ER_{stat}) of ER, obtained by MC simulation, are affected by a negligible error with respect to the intrinsic one. For this reason, these errors are omitted and the error on ER_{MC} is calculated only from the intrisic ER, $(4.5 \pm 0.5)\%$. The SR and ER values obtained correspond to the source position in the center area of the crystal. In the tables, SR_{lin}, SR_{qua} L_{lin} and L_{qua} represent the SR and the L obtained by applying

linear/quadratic (with threshold) algorithm.

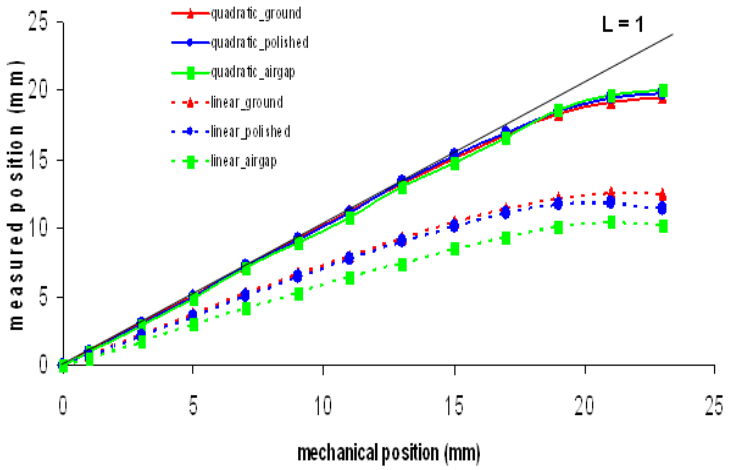

Figure 2.25: L values for the three setup described in the text. These values are obtained using either the "quadratic" or the "linear" algorithm.

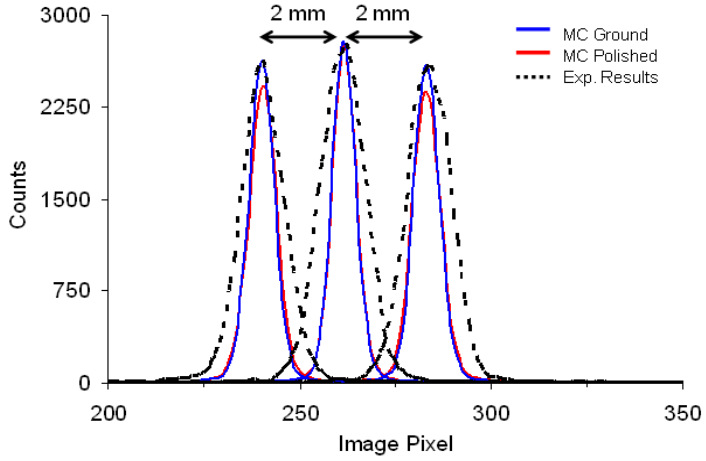

Figure 2.26: SR comparison between MC and experimental results.

Table 2.3: Photoelectrons and Energy Resolution

Setup	$< Nphe >$	ER_{sta} %	ER %
Exp.	-	-	9.0 ± 0.3
Polished	1047 ± 1	7.2	8.6 ± 0.3
Ground	1603 ± 1	5.9	7.4 ± 0.3
Air Gap	1137 ± 1	7.0	8.3 ± 0.3

Table 2.4: Spatial Resolution (central interaction)

Setup	SR_{lin} (mm)	SR_{qua} (mm)
Exp.	1.6 ± 0.1	1.1 ± 0.1
Polished	1.2 ± 0.1	0.77 ± 0.04
Ground	1.0 ± 0.1	0.75 ± 0.04
Air Gap	1.5 ± 0.1	0.8 ± 0.1

Table 2.5: Position Linearity

Setup	L_{lin} (mm/mm)	L_{qua} (mm/mm)
Exp.	0.65 ± 0.05	1.00 ± 0.05
Polished	0.67 ± 0.05	1.02 ± 0.05
Ground	0.70 ± 0.05	1.01 ± 0.05
Air Gap	0.55 ± 0.05	0.99 ± 0.05

The L coefficients (Table 2.5) are calculated not considering the last three values near the crystal border (Fig. 2.25). As we can see in the tables, the simulation results for "Polished" model, which corresponds to the crystal surface treatment made by St.

Gobain, show a reasonable agreement with experimental data in terms of ER, although the spatial resolution is better in the MC.

The differences in terms of SR between MC and experimental data, are probably imputable to a not complectly knowledge of the experimental surface proprieties of the crystal and consequently the impossibility to tune all the optical parameters of the surfaces. In particulary, we don't know the values of σ_α (as it has been calculated in [55] for BGO crystal), C_{sl}, C_{ss}, C_{bs} and C_{dl}. To tune exectly these parameters, it is experimentally necessary "to sacrifice" a $LaBr_3$:Ce (it is hygroscopic, fragile and very expensive) for a "deep" optical study. Experimentally, we have higher light background (mainly on the crystal edge) than MC and for this reason the SR experimental values are worse than those of the MC. Moreover, the ER difference between the experimental and the simulated value (Polished model) is also due to the presence of the intrinsic ER of PM that is not possible to simulate by MC.

In conclusion, $LaBr_3$:Ce crystals with a ground treatment of the lateral surfaces could pave the way to submillimeter spatial resolution, with high detection efficiency and optimal energy resolution.

This result are important for the future improvement of $LaBr_3$:Ce scintillation crystals machining.

The MC confirms also the expected intrinsic non-linearity of the reconstruction of the impact point of the photon into the crystal. Such a non-linearity is produced by the effect of the crystal edges on the light distribution.

A "quadratic" algorithm for the impact position reconstruction has been tested on the simulation and real data outputs. Such an algorithm is capable of improving the L, and hence the SR, of the final image of the radiation source.

Chapter 3

ECORAD

3.1 Introduction

To obtain a more reliable diagnosis, functional and anatomic information are often considered together. The visual quality and quantitative accuracy of radionuclide imaging, however, often lacks anatomic cues that are needed to localize or stage the disease and typically has poorer statistical and spatial characteristics than anatomic imaging methods, such as Magnetic Resonance Imaging (MRI), X rays or ultrasounds (US).

Among the techniques able to provide anatomical information, US are a cost-effective and reliable method. Further, US probes are one of the most common ways of assembling portable devices. These issues have motivated the development of a new approach that combines functional data from compact gamma cameras with structural data from US equipments. The ECORAD collaboration aims at developing a multi-modal portable camera that can acquire US and scintigraphic images at the same time. This will allow both morphological and functional information to be obtained with the same device. One of the final outcomes of the camera will be a 3D image which contains the fused information from the two modalities.

ECORAD is based on a large scientific collaboration:

- INFN sections of Bologna, Roma 1, Roma 3 and Legnaro.
- Physics Dpt. - Alma Mater Studiorum - University of Bologna.
- Experimental Medicine Dpt. "Sapienza" University of Rome.
- Physics Dpt., EDEMOM PhD School of Microelectronics - University of Rome3.
- Physics Dpt. - University of Padua.

By using previous experience in simulating systems for medical imaging described in Chapter 2, here we intend to perform a preliminary evaluation of the scintigraphic part of the camera, by means of simulations with GEANT4 (version 4.9.0).

3.2 Ultrasound probe design

US is a sound with frequency above about 20 kHz. Diagnostic US imaging uses much higher frequencies, in the order of megahertz. The frequencies present in usual sonograms can be anywhere between 2 and 13 MHz. A single focused arc-shaped sound wave, from the sum of all the individual pulses emitted by a transducer, is produced. Using a conventional diagnostic US device and a position sensing device, it is possible to create three dimensional US images.

The principle of operation is well-known: electrostatic transduction mechanism by using a Capacitive Micromachined Ultrasonic Transducer (CMUT). The basic element of a CMUT is a capacitor cell with a fixed electrode (backplate) and a free electrode (membrane). A voltage is applied between the membrane and the backplate. This voltage produces a membrane vibration with generation of ultrasounds. Conversely, when the membrane is subjected to an incident ultrasonic wave, the change of capacitance

can be detected as a current or voltage signal. A Direct Current (DC) bias voltage [57] must be used in reception for signal detection, and it is required in transmission for linear operation. In addition, both the transmit and receive sensitivities increase with increasing the bias voltage [58].

Two different US probes are usually used. B-scan US systems produce images which are perpendicular to the skin surface. C-scan systems can generate images which are parallel to the surface of the skin (coronal), see Fig. 3.1. C-scan ultrasound can be displayed in 2D or 3D US technique. 2D plane images, usually in gray scale, are recordable at different depths, maintaining high quality information.

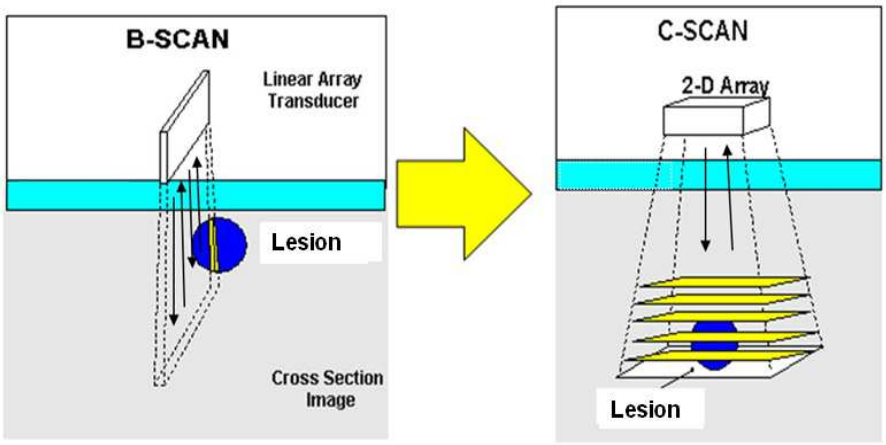

Figure 3.1: Differences in image registration between B-scan and C-scan US probe.

For our application, the US probe will be realized at the University of Roma III [59].

3.3 Scintigraphic camera

3.3.1 Slant collimator

The evaluation of the scintigraphic part of the camera starts by simulating the different geometry of collimators allowing for the improvement of system sensitivity to the photons from specific regions of the imaging space, and thus of the sensitivity to the organs-of-interest (OoIs) that fall into these regions. The most commonly used collimator geometry in SPECT is parallel-beam collimation [60].

Slant collimators have the remarkable feature of being capable to provide a 3D image even with a stationary gamma camera. A Rotating multi-segment slant-hole (RMSSH) SPECT system combines a conventional SPECT system with a slant collimator, and it represents a valid alternative to the SPECT modality in the case of limited FOV [61] [62]. Recently slant collimator have been used in gamma cameras for cardiac imaging [63]. Figures 3.2 and 3.3 show schematic representations of a rotating slant hole collimator.

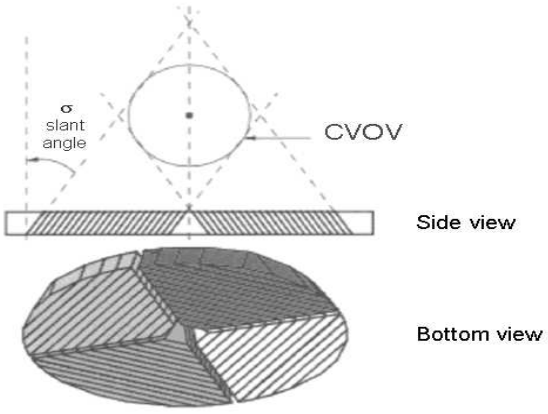

Figure 3.2: : A schematic representation of a rotating slant hole collimator, bottom. The Central Volume of Vision (CVOV), top.

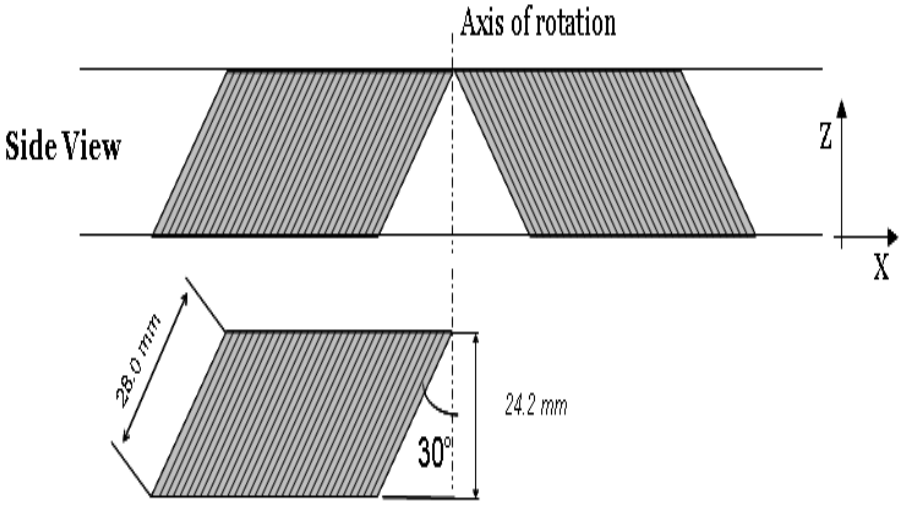

Figure 3.3: Side view of slant hole collimator.

During data acquisition, the RMSSH SPECT camera makes several stops. At each camera stop, the collimator rotates about its center axis to acquire multiple projections necessary for image reconstruction. The collimator design, based on a four-segment slant-hole collimator, is implemented by GEANT4. The major features of the simulated hexagonal holes slant collimator are reported in Table 3.1.

Table 3.1: Features of the simulated slant collimator with hexagonal holes.

Hole diameter	1.8 mm
Hole length	28 mm
Septa thickness	0.25 mm
Slant angle	30°
Sensitivity	512 cpm/μCi

A simple method to make an hexagonal holes slant collimator in GEANT4 does not

exist. To construct the collimator we have therefore started from a basic hexagonal hole. By two boolean operations (subtraction) [64] we have "cut" an hexagonal base prism with two inclined parallelepipeds respectively at the top and at the bottom as shown in Fig. 3.4. Then a rotation of the individual hole and an assembly operation (repeated copies) give us the final result after insertion in a lead block.

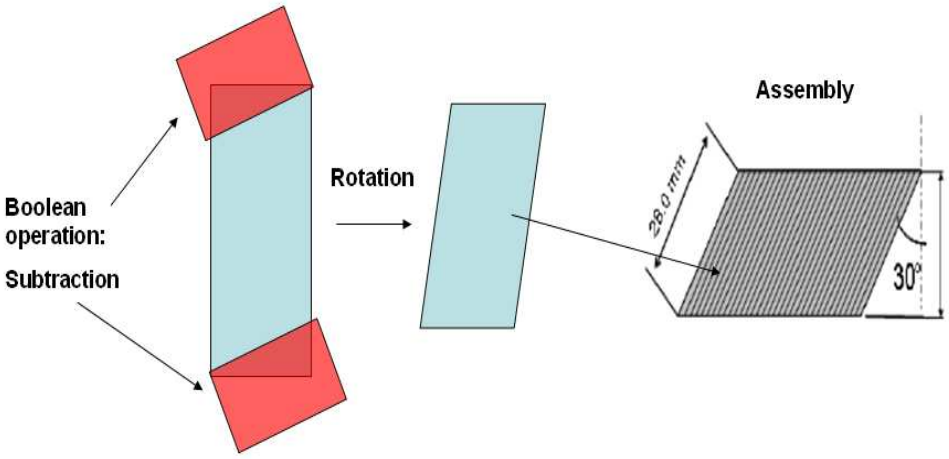

Figure 3.4: Sketch of slant construction.

The estimated sensitivity is about twice respect to a General Purpose (GP) collimator assembled on a standard gamma camera. The collimator characteristics have been decided in order to increase sensitivity rather than SR. In fact localization of the spatial lesion will be provided by the ultrasound probe; this solution permits to improve the gamma camera sensitivity and, by consequence, to enhance gamma-ray statistics and reduce scintigraphic time measurement.

Figure 3.5 shows the results of a simulated flood of 140 keV energy photons on a slant collimator.

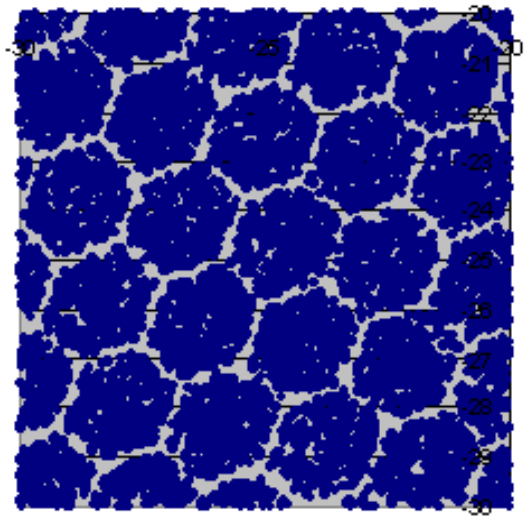

Figure 3.5: Hexagonal holes slant collimator. The image is obtained by a flood of 140 keV energy photons.

3.3.2 Simulation setup

There are two possible ways to couple collimator and crystal: a single crystal and a rotating collimator or a four crystal setting and the rotation of the entire system. In this Chapter the second one is described. Each segment of the quadri-slant collimator is coupled to a compact gamma camera. Figure 3.6 shows a schematic representation of a single detector segment. Each collimator segment is installed on the same detector (crystal + PM) described in Chapter 2. In this way, as clearly visible in Fig. 3.7, the dead area between two segments, due to the usage of slant collimators, is avoided. The four-segment collimator provides four projections of the object (one for each segment), for each position of the camera. More projections are gained by rotating the small gamma camera around the vertical axis (z). In this way, we are able to get various projections at different angles without the need of rotating the camera around the object.

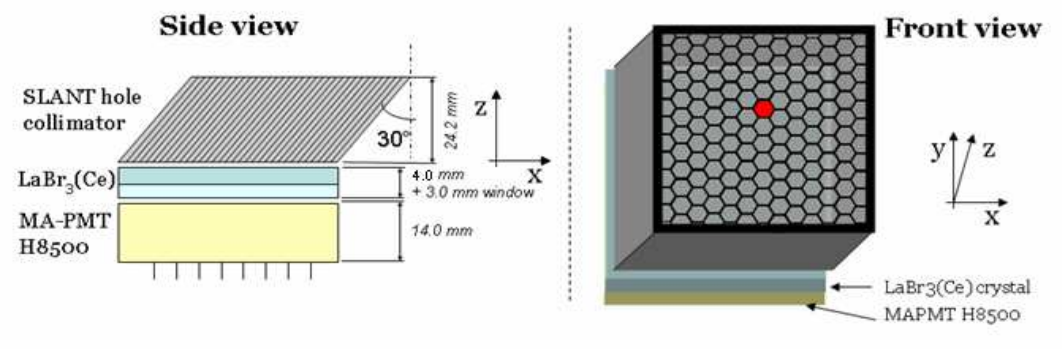

Figure 3.6: Schematic representation of a single detector segment.

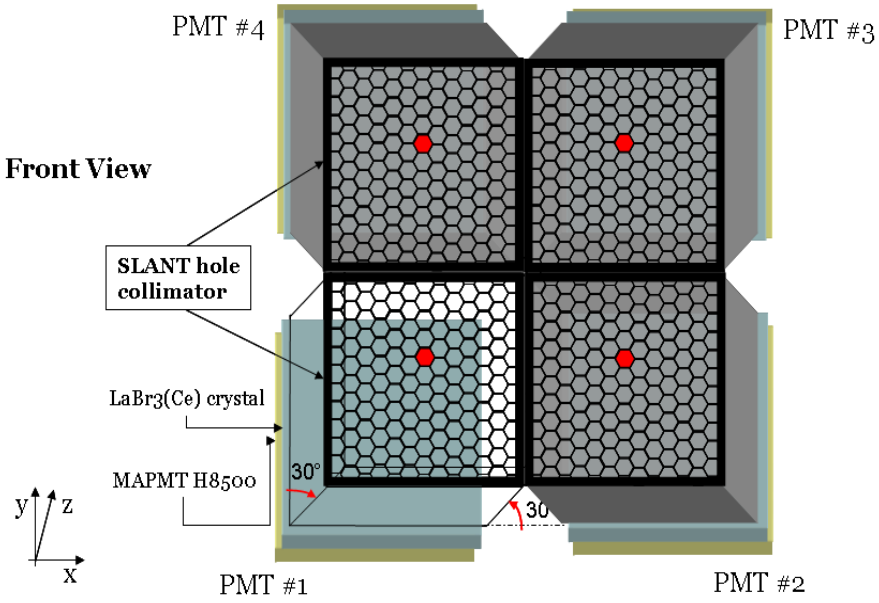

Figure 3.7: MC Simulation setup of quadri-slant hole scintigraphic detector.

Each segment of the camera provides a partial FOV of the investigated object. As a consequence, the total FOV of the scintigraphic camera is determined by the volume intersected by all the projections. Indeed, it is worth noticing that the remaining

volume is viewed by only a subset of the set of projections acquired. Therefore, details here will be imaged with less resolution and contrast. In our case, the FOV consists of the figure of rotation created from the rotation of the rhombus area shown in Fig. 3.8.

Size and position of the rhombus are determined by three parameters: the slant angle of the collimator, the size and the position of the camera. Hence, in order to change the FOV one can act modifying their values. The position of each event registered by the camera has been estimated by the centroid of the charge distribution within the PM by using the "quadratic" algorithm described in Section 2.4. A visualization sketch, using GEANT4, of the complete simulation setup is shown in Fig. 3.9. The information about the depth localization of the lesions is recovered by performing a tomographic reconstruction starting from the planar images. The 3D images are reconstructed with a back-projection technique [65]. We have reconstructed the volumetric images with cubic voxels with a side of 1 mm.

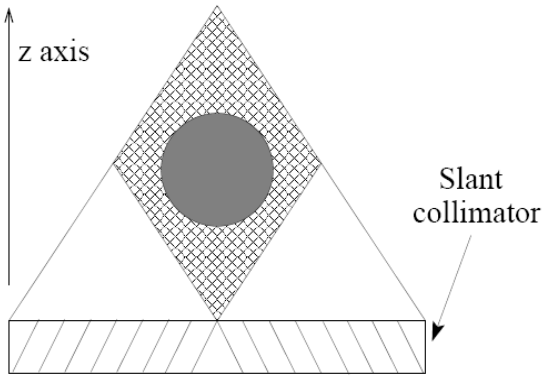

Figure 3.8: Sketch of a lateral projection of the slant- collimator based camera. The FOV of the camera is represented by the area filled with squared pattern and is determined by the slant angle and the size of the camera.

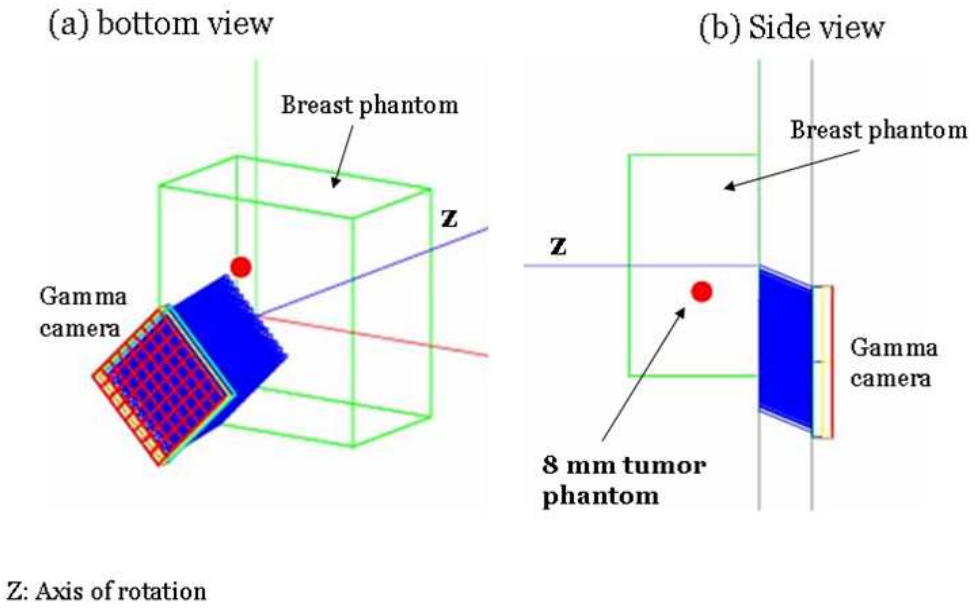

Figure 3.9: Simulation setup by GEANT4: a breast phantom positioned in front of a single gamma camera segment.

3.4 Experimental setup

A schematic representation of the assembling for the echo-scintigraphic system is illustrated in Fig. 3.10. The US probe will run along the collimator surface and its movement will be possible thanks to a step motor having about 0.1 mm steps with digital controller, suitable for the tomographic resolution. An impedance adapter guarantees the acoustic coupling between the probe and the phantom. On the gamma camera, there is an airtight box that contains the echographic gel. The slant hole collimator will rotate at established steps to enable the 3D reconstruction.

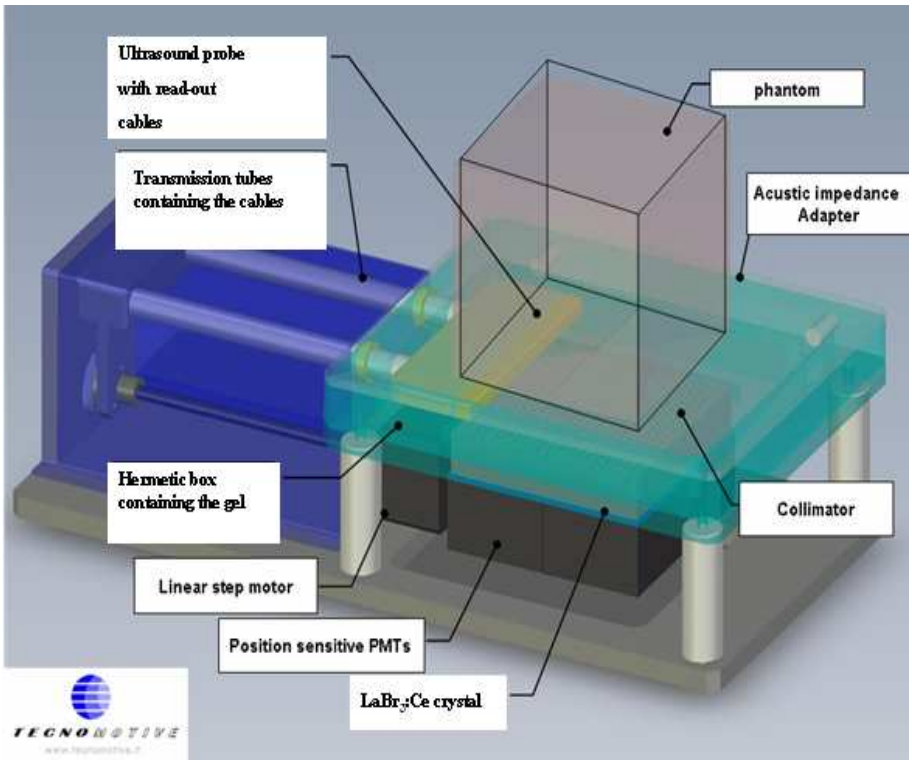

Figure 3.10: Sketch of the echo-gamma detector.

3.5 Simulation results

In the first simulation, a radioactive point-like source is placed, in air, at different distances from the collimator. Figure 3.11 shows an example of the reconstruction of three point sources located on the central axis at different distances from the collimator. In this case, the three sources are simulated together, thus we can establish whether our system is able to discriminate sources positioned at different depths. The same picture illustrates both the reconstructed slices at the depth where the source is supposed to be located and a profile along the z axis. It is worth noticing that the SR is better for sources close to the collimator, as expected. Further, we can state that the depth

resolution of the system is accurate enough to distinguish point sources spaced apart at a distance of 2 cm, at least for depths up to 5 cm from the camera.

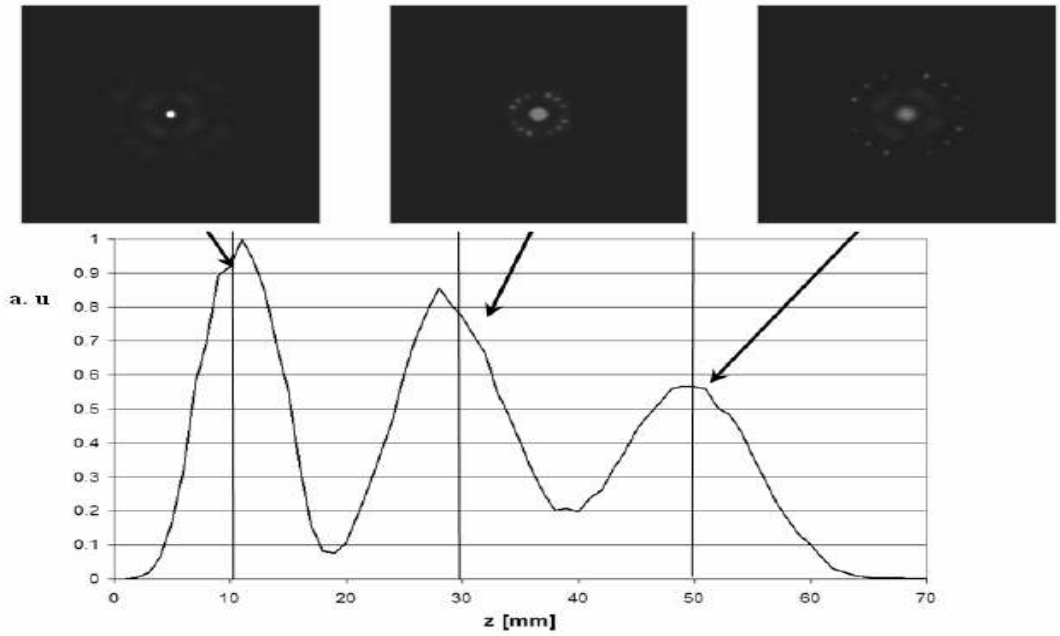

Figure 3.11: Reconstruction of three point sources located on the z axis at a distance of 1 cm, 3 cm, and 5 cm from the collimator. Top: reconstructed slices at depth 1 cm, 3 cm, and 5 cm. Bottom: z profile of the reconstructed volume estimated on a central ROI.

In order to give a more complete assessment of the SR of the system across the entire FOV, we simulated point sources located at different depths and positioned on the central axis and on axes at a certain distance from the central one. In this case, we reconstructed each point source separately. Figure 3.12 shows a plot of the FWHM of some of the simulated sources. As expected, the axial FWHM is worse (about double) than the planar one. Besides, the SR clearly gets worse for points outside the FOV. We have also simulated a phantom consisting of a cube made of soft-equivalent tissue with dimension $6 \times 6 \times 10$ cm^3. In order to emulate a clinical examination, we simulated

the number of photons emitted in a total imaging time of 10 minutes.

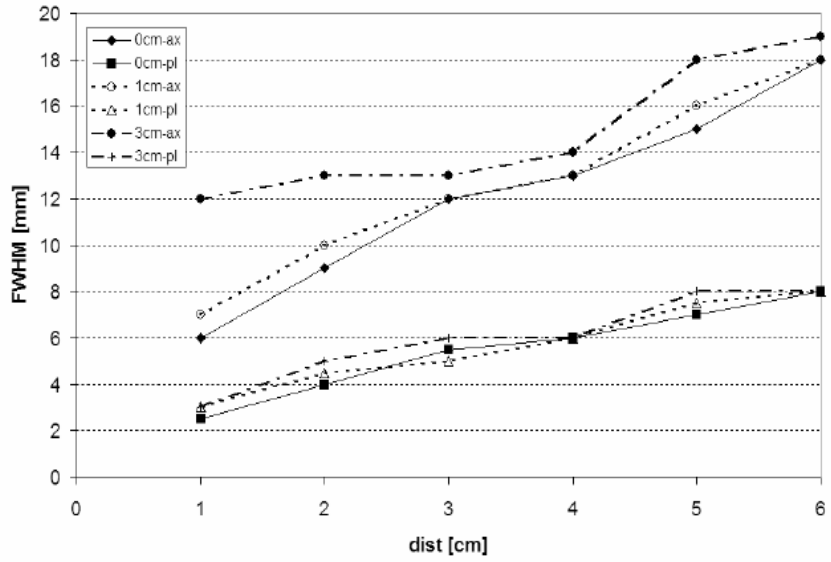

Figure 3.12: Axial and planar SR (as FWHM) of the reconstructed point sources, as a function of the distance from the collimator. Sources are located on the central axis (0 cm), and on two lateral positions with a distance of 1 cm and 3 cm from the central axis.

We have simulated 16 projections, corresponding to four different positions of the four-segment camera. Photons have energy equal to 140 keV, typical for the most common radioisotope used in SPECT applications (i.e ^{99m}Tc). The simulated background activity is fixed to 100 nCi/cc, and spherical tumors with a diameter of 8 mm and 10 mm were inserted within the phantom at a distance of 3 cm from the collimator. We simulated various Tumor/Background (T/B) ratios, ranging from 8:1 to 20:1. For each reconstruction of the phantom we calculated the Signal-to-Noise Ratio (SNR) on a ROI centered over the simulated tumor, in order to assess the quality of the reconstructed image. Figures 3.9 and 3.13 show this simulation setup.

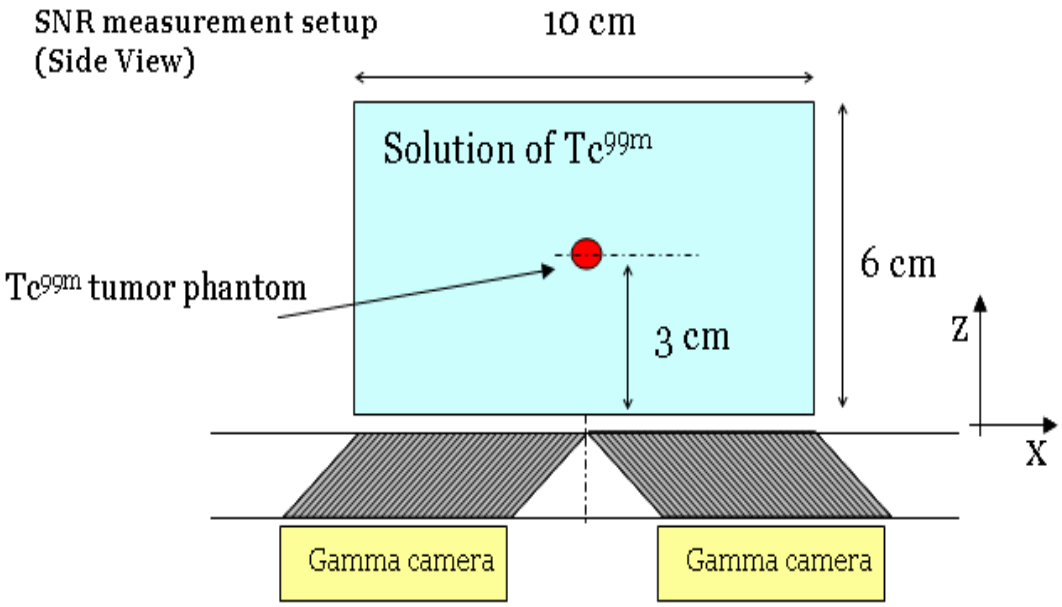

Figure 3.13: Simulation setup for SNR measurement.

The SNR is calculated according to equation

$$SNR = \frac{M_{tum} - M_{BKG}}{\sigma_{BKG}} \tag{3.1}$$

where M is the average amount of counts in a selected ROI, M_{tum} related to tumor activity and M_{BKG} in the respective outer area.

Table 3.2 shows some SNR values calculated for the 8 mm and 10 mm tumors located at 3 cm from the collimator. By assuming the standard detection limit of SNR equal to 5, we can note that the 8 mm tumor is visible for T/B ratios greater than 15:1, whereas the 10 mm tumor is perceptible also for smaller T/B values. Thanks to the slant collimators, we thus demonstrate the feasibility of detecting small tumors with a camera able to trace the depth of a lesion, without the need of rotating around the body.

Table 3.2: SNR values for 8 mm and 10 mm tumors located at 3 cm from the collimator for different T/B values.

T/B	8:1	10:1	15:1	20:1
8 mm	3.0 ± 0.3	3.2 ± 0.3	5.4 ± 0.5	6.7 ± 0.7
10 mm	3.7 ± 0.4	5.5 ± 0.6	8.6 ± 0.9	9.2 ± 0.9

The proposed camera based on slant collimators is able to distinguish point sources located at a distance of about 2 cm, if within the FOV of the camera.

The first preliminary results seem to show that for a 10 minutes examination the visibility limit of the camera is about 15:1 T/B for the 8 mm tumor and 10:1 T/B for the 10 mm tumor located at 3 cm from collimator. We believe that this remarkable feature could represent an important advance for the development of portable devices dedicated to the imaging of lesions located at small depths (up to a few centimeters).

Future studies will concern:

- SNR analysis vs time of measurement; the goal will be to evaluate the shortest time necessary to obtain significant images in diagnostics.
- SNR analysis vs the number of rotations and capture time on equal terms with total time.
- Deciding the costs between the two configurations of revelation: we will have to choose between a single crystal and a rotating collimator or a four crystal setting and the rotation of the entire system.

Conclusions

The dosimetry of panels of tumor cell lines irradiated with ^{188}Re and medical imaging prototypes development, based on $LaBr_3$:Ce scintillation crystals, have been studied using GEANT4 simulations.

The dosimetry simulations estimate an average energy deposition in the biological sample of about 280 eV per ^{188}Re decay event. The dose absorbed in 48 h (72 h) by each of the cell cultures deposited in the wells, when the activity of the radioactive solution is 50 μCi/cc, is about 6.3 Gy (6.9 Gy).

A MC simulation of a $LaBr_3$:Ce crystal coupled with a position sensitive multi-anode photomultiplier has been performed. The simulation parameters have been tuned to adapt the light distribution in the anode read-out to the experimental one obtained with a continuous $LaBr_3$:Ce crystal.

The results of the simulation for the "Polished" model of the $LaBr_3$:Ce crystal, which corresponds to the experimental crystal surface treatment, show a reasonable agreement with experimental data in terms of ER at 140 keV.

The MC confirms also the expected intrinsic non-linearity of the reconstruction of the impact point of the photon into the crystal. Such a non-linearity is produced by the effect of the crystal edges on the light distribution. A "quadratic" algorithm for the impact position reconstruction has been tested on the simulation and real data

outputs. Such an algorithm has been found capable of improving the L, and hence the SR, of the final image of the radiation source.

Having tested, in the simulation, surface treatments different from the one applied to the crystal used in our experimental measurements, we found out that ER and SR could be improved, in principle, by machining in a different way the lateral surfaces of the crystal. In particular, we conclude that $LaBr_3$:Ce crystals with ground lateral surfaces could pave the way to submillimeter SR, with high detection efficiency and optimal ER.

We have then studied a system able to acquire both echographic and scintigraphic images to let the medical operator obtain the complete anatomic and functional information for tumor diagnosis. The characteristics of the gamma camera are described by the same simulation as mentioned above. The scintigraphic part of the detector is analyzed and first attempts to reconstruct tomographic images have been made using as method of reconstruction a standard back-projection algorithm.

The proposed camera based on slant collimators is able to distinguish point sources, if within the FOV of the camera, located in air at a distance of about 2 cm from each other.

In particular conditions of uptake, tumor depth and dimension, the preliminary results show that the SNR values obtained are higher than the standard detection limit.

The dual modality portable device based on the $LaBr_3$:Ce continuous gamma camera and an ultrasound probe can permit a very attractive trade-off among SR, sensitivity and detection field of view for many imaging tasks. This aspect is especially true for imaging organs at short distance from the collimator, as far as for breast and tyroid.

Papers

A. Antoccia, G. Baldazzi, M. Bello, D. Bernardini, P. Boccaccio, D. Bollini, D. Camporese, F. De Notaristefani, **S. Lo Meo**, U. Mazzi, L. Melendez Alafort, G. Moschini , F.L. Navarria, V. Orsolini Cencelli, G. Pancaldi, R. Pani, R. Pellegrini, A. Perrotta, A. Rosato, A. Sgura, C. Tanzarella, N. Uzunov, M. Zuffa, *"Simulations and test for metabolic radiotherapy with* ^{188}*Re"*, Nuclear Physics B (Proc. Suppl) **172** (2007) 303-307.

R. Pani, M. N. Cinti, R. Pellegrini, P. Bennati, **S. Lo Meo**, S. Ridolfi, F. Vittorini, F. de Notaristefani and M. Mattioli, *" Photodetector and scintillation crystals requirements for Gamma Ray Imaging."* Il Nuovo Cimento, **30C**, 5, (2008), pp. 435-448.

Lo Meo S, Lanconelli N., Navarria F. L., Pani R., Pellegrini R., A. Perrotta, *"A GEANT4 simulation code for simulating optical photons in SPECT scintillation detectors"* 4th International Conference on Imaging Technologies in Biomedical Sciences, 22-28 September 2007, Milos Conference Center G. Eliopoulos, Milos Island (Greece).- to be published on Nucl. Instrum. Meth A.

S. Lo Meo, G. Baldazzi, P. Bennati, D. Bollini, V. O. Cencelli, M. N. Cinti, N. Lanconelli, G. Moschini, F. L Navarria, R. Pani, R. Pellegrini, A. Perrotta and F. Vittorini, *"GEANT4 Simulation for Modelling the Optics of* $LaBr_3$*:Ce Scintillation Imagers"*, accepted at IEEE MIC Conference 2008.

S. Lo Meo, N. Lanconelli, F.L. Navarria, A. Perrotta, G. Baldazzi, D. Bollini, R. Pani, R. Pellegrini, M.N. Cinti, P. Bennati, G. Moschini, P. Boccaccio, V. Orsolini Cencelli, *"A dual modality ultrasound-gamma system: Monte Carlo simulations of the scintillation imager"* - iWoRiD'08 Conference, Porvoo, Finland, June 29th, 2008 - to be published on Nucl. Instrum. Meth A.

S. Lo Meo, G. Baldazzi, P. Bennati, D. Bollini, V. O. Cencelli, M. N. Cinti, G. Moschini, N. Lanconelli, F. L. Navarria, R. Pani, R. Pellegrini, A. Perrotta, F. Vit-

torini, *"Optical Physics of Scintillation Imagers by GEANT4 Simulation"* - iWoRiD'08 Conference, Porvoo, Finland, June 29th, 2008 - to be published on Nucl. Instrum. Meth A.

S. Lo Meo, N. Lanconelli, F.L. Navarria, A. Perrotta, G. Baldazzi, D. Bollini, R. Pani, R. Pellegrini, M.N. Cinti, P. Bennati, G. Moschini, P. Boccaccio, V. Orsolini Cencelli, *"A dual modality ultrasound-gamma system: first preliminary results of the scintigraphic camera"*, IPRD08- Siena- October 2008, to be published on Nuclear Physics B (Proc. Suppl).

Pani R., Cinti M. N., Pellegrini R., Bennati P., Ridolfi S., Mattioli M., Scafé R., Pisacane F., Baldazzi G., Navarria F., **Lo Meo S.**, Moschini G., Orsolini Cancelli V, *"Ultra High Quantum Efficiency PMT for energy resolution measurements of $LaBr_3$:Ce scintillation crystals"*- NDIP2008 Conference, Aix-les-Bains, France, June 15-20, 2008 - to be published on Nucl. Instrum. Meth A.

R. Pani, R. Pellegrini, P. Bennati, M. N. Cinti, S. Ridolfi, R. Scafé, G. De Vincentis, **S. Lo Meo**, N. Lanconelli, F. Navarria, G. Moschini, A. Fabbri, E. D'Abramo, D. Sacco, V. Orsolini Cencelli and F. de Notaristefani, *"A novel parallel hole collimator for high resolution SPET imaging with a compact $LaBr_3$:Ce gamma camera"* - accepted at IEEE MIC Conference 2008.

R. Pani, M. N. Cinti, R. Scafé, P. Bennati, R. Pellegrini, F. Vittorini, S. Ridolfi, **S. Lo Meo**, M. Mattioli, G. Baldazzi, G. Trotta, F. Navarria, G. Moschini, and V. Orsolini Cencelli, *"Gamma ray spectroscopy with $LaBr_3$:Ce scintillation crystals coupled to an Ultra High Quantum Efficiency PMT"* - submitted to IEEE NSS Conference 2008.

R. Pani, R .Pellegrini, P. Bennati, M. N. Cinti, F. Vittorini, R. Scafé, **S. Lo Meo**, F. Navarria, G. Moschini, V. Orsolini Cencelli, F. De Notaristefani and P. Russo, *"High spatial and energy resolution gamma imaging based on $LaBr_3$:Ce continuous crystals"* - submitted to IEEE NSS Conference 2008.

Appendix A

GEANT4 Optical Physics

A.1 Optical photons

A photon is considered to be optical when its wavelength is much greater than the typical atomic spacing. In GEANT4 optical photons are treated as a class of particles distinct from their higher energy gamma cousins. This implementation allows the wave-like properties of electromagnetic radiation to be incorporated into the optical photon process. Because this theoretical description breaks down at higher energies, there is no smooth transition as a function of energy between the optical photon and gamma particle classes. For the simulation of optical photons to work correctly in GEANT4, they must be imputed a linear polarization. This is unlike most other particles in GEANT4 but is automatically and correctly done for optical photons that are generated as secondaries by existing processes in GEANT4.

It is possible to start optical photons as primary particles but in this case, the user must set the linear polarization using particle gun methods, the General Particle Source, or her/his PrimaryGeneratorAction. For an unpolarized source, the linear polarization should be sampled randomly for each new primary photon. The

GEANT4 catalogue of processes at optical wavelengths includes refraction and reflection at medium boundaries, bulk absorption, Rayleigh scattering and wavelength shifting. Processes which produce optical photons include the Cerenkov effect, transition radiation and scintillation. It is possible for the user to add as many material (optical) properties to the material as he wishes using the methods supplied by the G4MaterialPropertiesTable class.

A.2 Scintillation process

Scintillation is a flash of light produced in a transparent material by an ionization event. This light is produced by a a substance (scintillator) that absorbs high energy (ionizing) electromagnetic or charged particle radiation and then, in response, fluoresces photons at a characteristic wavelength, releasing the previously absorbed energy. Scintillators are defined by their light output (number of emitted photons per unit absorbed energy), fast and slow decay times, and optical transparency at wavelengths of their own specific emission energy. Hence, every scintillating material has a characteristic light yield, ($SCINTILLATIONYIELD$), and an intrinsic resolution, ($RESOLUTIONSCALE$), which generally broadens the statistical distribution of generated photons. A wider intrinsic resolution is due to impurities which are typical for doped crystals like NaI:Tl and CsI:Tl. On the other hand, the intrinsic resolution can also be narrower when the Fano factor plays a role. The actual number of emitted photons (Np) during a step fluctuates around the mean number of photons with a width given by:

$$\Delta Np = RESOLUTIONSCALE \times \sqrt{MeanNumberOfPhotons} \tag{A.1}$$

The "$MeanNumberOfPhotons''$ has a linear dependence on the local energy de-

position, but it may be different for minimum ionizing and non-minimum ionizing particles. A scintillator is also characterized by its photon emission spectrum and by the exponential decay of its time spectrum. In GEANT4 the relative strength of the fast component ($FASTCOMPONENT$) as a fraction of total scintillation yield is given by the $YIELDRATIO$. Scintillation may be simulated by specifying these empirical parameters for each material. In the user's DetectorConstruction class, it is also necessary to fix the relative spectral distribution, as a function of photon energy for the scintillating material, the refraction index ($RINDEX$) and the absorption lenght ($ABSLENGHT$) as shown in Fig. A.1.

```
const G4int LaBr_NUMENTRIES = 4;
G4double LaBr_Energy[LaBr_NUMENTRIES]    = { 3.001*eV, 3.000*eV, 2.999*eV, 2.998*eV };
G4double LaBr_FAST[LaBr_NUMENTRIES] = { 1.0 , 1.0, 1.0, 1.0 };
G4double LaBr_RIND[LaBr_NUMENTRIES]  = { 1.9 , 1.9, 1.9, 1.9 };
G4double LaBr_ABSL[LaBr_NUMENTRIES]  = { 35.0*cm , 35.0*cm, 35.0*cm, 35.0*cm };
G4MaterialPropertiesTable* LaBr_MPT = new G4MaterialPropertiesTable();
LaBr_MPT->AddProperty("FASTCOMPONENT", LaBr_Energy, LaBr_FAST, LaBr_NUMENTRIES);
LaBr_MPT->AddProperty("RINDEX",        LaBr_Energy, LaBr_RIND, LaBr_NUMENTRIES);
LaBr_MPT->AddProperty("ABSLENGTH",     LaBr_Energy, LaBr_ABSL, LaBr_NUMENTRIES);
LaBr_MPT->AddConstProperty("SCINTILLATIONYIELD", 63000./MeV);
LaBr_MPT->AddConstProperty("RESOLUTIONSCALE",1.0);
LaBr_MPT->AddConstProperty("FASTTIMECONSTANT",16.*ns);
targetMaterial->SetMaterialPropertiesTable(LaBr_MPT);
```

Figure A.1: $LaBr_3$:Ce optical properties. All values are taken from St. Gobain [46] Data Sheet.

A.3 Tracking optical photons

A.3.1 Absorption

The implementation of optical photon bulk absorption, G4OpAbsorption, is trivial in that the process merely kills the particle. The procedure requires the user to fill

the relevant G4MaterialPropertiesTable with empirical data for the absorption length, using $ABSLENGTH$ as the property key in the public method AddProperty. The absorption length is the average distance traveled by a photon before being absorpted by the medium; i.e. it is the mean free path returned by the GetMeanFreePath method.

A.3.2 Rayleigh scattering

The differential cross section in Rayleigh scattering, $d\sigma/d\omega$, is proportional to $1 + cos^2(\theta)$, where θ is the polar of the new polarization vector with respect to the old polarization vector. The G4OpRayleigh scattering process samples this angle accordingly and then calculates the scattered photon's new direction by requiring that it be perpendicular to the photon's new polarization in such a way that the final direction, initial and final polarizations are all in one plane. This process thus depends on the particle's polarization. The photon's polarization is a data member of the G4DynamicParticle class. A photon which is not assigned a polarization at production, either via the SetPolarization method of the G4PrimaryParticle class, or indirectly with the SetParticlePolarization method of the G4ParticleGun class, may not be Rayleigh scattered.

Scintillation photons have a random linear polarization perpendicular to their direction. The process requires a G4MaterialPropertiesTable to be filled by the user with Rayleigh scattering length data. The Rayleigh scattering attenuation length is the average distance traveled by a photon before it is Rayleigh scattered in the medium and it is the distance returned by the GetMeanFreePath method. The G4OpRayleigh class provides a RayleighAttenuationLengthGenerator method which calculates the attenuation coefficient of a medium following the Einstein-Smoluchowski formula whose derivation requires the use of statistical mechanics, includes temperature, and depends on the isothermal compressibility of the medium. This generator is convenient when the Rayleigh attenuation length is not known from measurement but may be calculated

from first principles using the above material constants.

A.3.3 Boundary process

For the simple case of a perfectly smooth interface between two dielectric materials, all the user needs to provide are the refractive indices of the two materials stored in their respective G4MaterialPropertiesTable. In all other cases, the optical boundary process [66] design relies on the concept of surfaces. The information is split into two classes. One class in the material category keeps information about the physical properties of the surface itself, and a second class in the geometry category holds pointers to the relevant physical and logical volumes involved and has an association to the physical class.

Surface objects of the second type are stored in a related table and can be retrieved by either specifying the two ordered pairs of physical volumes touching at the surface, or by the logical volume entirely surrounded by this surface. The former is called a border surface while the latter is referred to as the skin surface. This second type of surface is useful in situations where a volume is coded with a reflector and is placed into many different mother volumes. A limitation is that the skin surface can only have one and the same optical property for all of the enclosed volume's sides.

The border surface is an ordered pair of physical volumes, so in principle, the user can choose different optical properties for photons arriving from the reverse side of the same interface. For the optical boundary process to use a border surface, the two volumes must have been positioned with G4PVPlacement. The ordered combination can exist at many places in the simulation. When the surface concept is not needed, and a perfectly smooth surface exists between two dielectric materials, the only relevant property is the index of refraction, a quantity stored with the material, and no restriction exists on how the volumes are positioned. The physical surface object also

specifies which model the boundary process should use to simulate interactions with that surface. In addition, the physical surface can have a material property table all its own. The usage of this table allows all specular constants to be wavelength dependent.

In case the surface is painted or wrapped (but not a cladding), the table may include the thin layer's index of refraction. This allows the simulation of boundary effects at the intersection between the medium and the surface layer, as well as the Lambertian reflection at the far side of the thin layer. This occurs within the process itself and does not invoke the G4Navigator.

Combinations of surface finish properties, such as polished or ground and front painted or back painted, enumerate the different situations which can be simulated.

The Polished model is meant to account for a perfectly polished surface. Photons incident on the surface are assumed to have random polarization, and are first tested for the possibility of Fresnel reflection if a change in refractive index occurs at the surface. The value of Reflectivity (R) is given by eq. A.2:

$$R = \frac{1}{2}\Big[\frac{sin^2(\theta_i' - \theta_t')}{sin^2(\theta_i' + \theta_t')} + \frac{tan^2(\theta_i' - \theta_t')}{tan^2(\theta_i' + \theta_t')}\Big] \tag{A.2}$$

where θ_i' and θ_i' are respectively the angle of incident and refraction with respect to a local micro facet's normal. If reflection occurs, the angle of reflection is set equal to the angle of incidence.

Figure A.2 shows all parameters needed for a complete optical description of the boundary process.

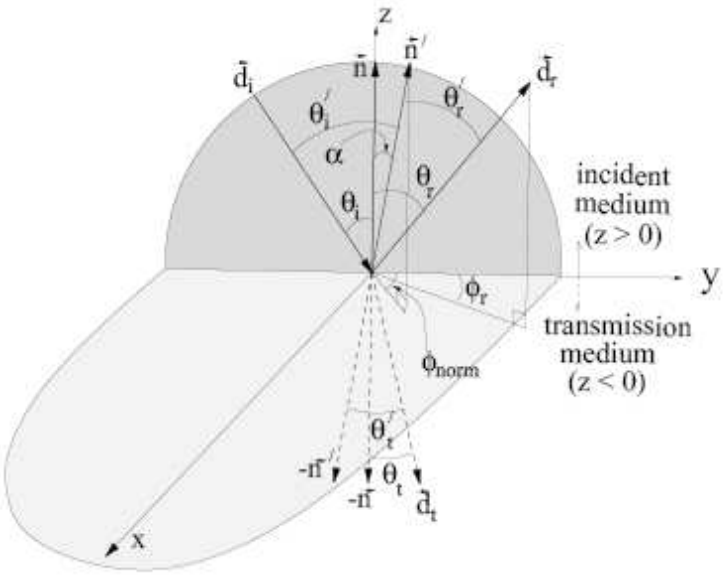

Figure A.2: Definition of geometric - optical parameters.

- n_1 - the index of refraction of the first medium,
- n_2 - the index of refraction of the second medium,
- $\vec{n}$ - the average normal of the surface,
- θ_i - the angle of incidence relative to the average normal,
- θ_r - the angle of reflection with respect to the average normal,
- θ_t - the angle of refraction with respect to the average normal,
- ϕ_r - the angle between the projection of the reflected or refracted photon onto the average surface and the plane of incidence,
- $\vec{n'}$ - the normal of a particular micro-facet,

- α - the angle between a given micro-facet and the mean surface,
- ϕ_{normal} - the angle between the projection of the micro-facet normal onto the average surface and the plane of incidence,
- θ_i' - the angle of incidence relative to the micro-facet normal,
- θ_r' - the angle of reflection with respect to the micro-facet normal,
- θ_t' - the angle of refraction with respect to the micro-facet normal.

If reflection does not occur, the optical photon is transmitted and assumed to follow Snell's Law of refraction. Depending on the refractive index change and the angle of incidence, may result in total internal reflection of the optical photon back into the the first medium.

Finally, the Ground option is avaible to simulate a roughened or ground optical surface. It is treated in the same way as the polished surface described above, except that the angle, α, between a given micro facet and the mean surface used to define θ_i' and θ_i' in eq. A.2 follows a Lambertian distribution.

When a photon arrives at a medium boundary its behavior depends on the nature of the two materials that join at that boundary. Medium boundaries may be formed between two dielectric materials or a dielectric and a metal. In the case of two dielectric materials, the photon can undergo total internal reflection, refraction or reflection, depending on the photon's wavelength, angle of incidence, and the refractive indices on both sides of the boundary. Furthermore, reflection and transmission probabilities are sensitive to the state of linear polarization. In the case of an interface between a dielectric and a metal, the photon can be absorbed by the metal or reflected back into the dielectric or detected with a detection $EFFICIENCY$ (that yields from 0.0 to 1.0) that emulates the quantum efficiency of a PM. Figure A.3 shows how can be set all UNIFIED parameters to simulate a PM surface with QE equal to 0.27.

```
G4OpticalSurface* OpSurface = new G4OpticalSurface("Glass_PM");
G4double sigma_alpha = 0.0;
OpSurface -> SetType(dielectric_metal);
OpSurface -> SetModel(unified);
OpSurface -> SetFinish(polished);
OpSurface -> SetSigmaAlpha(sigma_alpha);
G4double reflectivity[LaBr_NUMENTRIES] = {0.0 , 0.0, 0.0, 0.0};
G4double efficiency[LaBr_NUMENTRIES] = {0.27, 0.27, 0.27, 0.27};
G4MaterialPropertiesTable *Glass_sf = new G4MaterialPropertiesTable();
Glass_sf->AddProperty("REFLECTIVITY",LaBr_Energy,reflectivity,LaBr_NUMENTRIES);
Glass_sf->AddProperty("EFFICIENCY",LaBr_Energy,efficiency,LaBr_NUMENTRIES);
OpSurface -> SetMaterialPropertiesTable(Glass_sf);
new G4LogicalBorderSurface("Glass_SiPM", Glass, Check, OpSurface);
```

Figure A.3: PM surface proprieties

As expressed in Maxwell's equations, Fresnel reflection and refraction are intertwined through their relative probabilities of occurrence. Therefore neither of these processes, nor total internal reflection, are viewed as individual processes deserving separate class implementation. Nonetheless, an attempt is made to adhere to the abstraction of having independent processes by splitting the code into different methods where practicable.

One implementation of the G4OpBoundaryProcess class employs the UNIFIED [55] model of the DETECT [67] program. It applies to dielectric-dielectric and dielectric-metal interfaces and tries to provide a realistic simulation, which deals with all aspects of surface finish and reflector coating. The surface may be assumed as smooth and covered with a metallized coating representing a specular reflector with given reflection coefficient, or painted with a diffuse reflecting material where Lambertian reflection occurs. The surfaces are made up of micro-facets, with normal vectors that follow given distributions around the nominal normal for the volume at the impact point. For rough surfaces, it is possible for the photon to inversely aim at the same surface again after reflection of refraction and so multiple interactions with the boundary are

possible within the process itself and without the need for relocation by G4Navigator.

The UNIFIED model provides for a range of different reflection mechanisms. The specular lobe constant (C_{sl}) represents the reflection probability about the normal of a micro facet. The specular spike constant (C_{ss}), in turn, illustrates the probability of reflection about the average surface normal. The diffuse lobe constant (C_{dl}) is for the probability of internal Lambertian reflection, and finally the back-scatter spike constant (C_{bs}) is for the case of several reflections within a deep groove with the ultimate result of exact back-scattering (see Fig. A.4). The four probabilities must add up to one, with the diffuse lobe constant being implicit in the code.

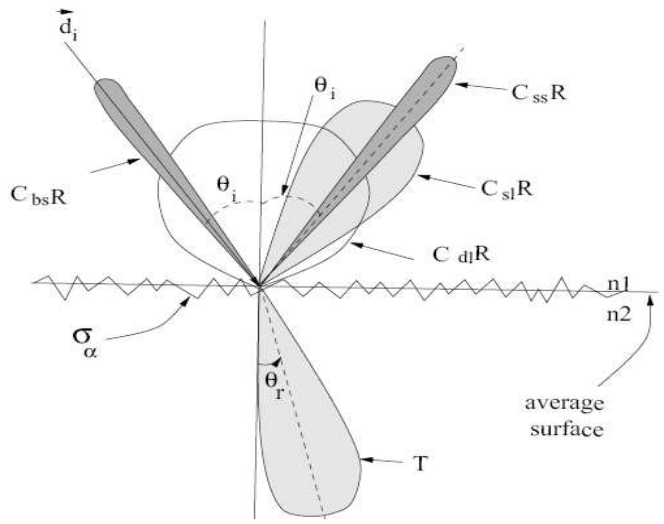

Figure A.4: Polar plot of the radiant intensity in the UNIFIED model

The different reflection mechanisms described till now, can be used in function of which kind of interface must be simulated. In fact, if there is an dielectric-dielectric interface with ground finish, for the user it is possible to set C_{sl}, C_{ss}, C_{bs} and C_{dl} but not the R value. With polish option there are only Fresnel Reflection, Refraction and Total Internal Reflection, so for the user it is not possible to use any constants. In the

case of dielectric-metal interface with ground finish, it is possible for the user to set all four constants. Finally, with polish option, the user can set R value, but it is possible only Spike Reflection ($C_{ss} = 1$).

Appendix B

Acronyms

^{188}Re	Rhenium-188
^{99m}Tc	Technetium-99m
^{188}Os	Osmium-188
BGO	Bismuth germinate
BNC	Binucleated Cells
CG	The glass protecting the crystal
CMUT	Capacitive Micromachined Ultrasonic Transducer
CsI:Tl	Cesium Iodide doped with Thallium
CVOV	Central Volume of Vision
DAPI	4'-6-Diamidino-2-phenylindole
DNA	DeoxyriboNucleic Acid
DC	Direct Current
EPDL	Evaluated Photon Data Library
EEDL	Evaluated Electron Data Library
EADL	Evaluated Atomic Data Library
ENSDF	Evaluated Nuclear Structure Data File

EC	Electron Capture
FITC	Fluorescein IsoThioCyanate
FOV	Field Of View
FWHM	Full Width Half Maximum
GEANT	GEometry ANd Tracking
GP	General Purpose
GPS	G4GeneralParticleSource
HA	Hyaluronic Acid
ID	Injected Dose
INFN	The National Institute of Nuclear Physics
ISS	Italian Istitute of Health
L	Linearity
$LaBr_3$:Ce	Lanthanum Bromide doped with Cerium
LSO	Lutetium oxy-orthosilicate
LY	Light Yield
MA-PMT	The 8×8 anodic array of the H8500
MC	Monte Carlo
MN	Micro Nuclei
MRI	Magnetic Resonance Imaging
MTT	3-(4,5-dimethylthiazol-2-yl)-2,5-diphenyltetrazolium bromide
NaI:Tl	Sodium Iodide doped with Thallium
NM	Nuclear Medicine
OoIs	organs-of-interest
PC	Personal computer
PET	Positron Emission Tomography
PM	Photomultiplier
PMG	Photomultiplier Glass

PSF	Point Spread Function
QE	Quantum Efficiency
R	Reflectivity
RMSSH	Rotating multi-segment slant-hole
SPECT	Single Photon Emission Computed Tomography
SNR	Signal-to-Noise
T/B	Tumor/Background
TUNEL	Terminal deoxynucleotidyl Transferase Biotin-dUTP Nick End Labeling
US	Ultrasound
YAP	Yttrium Aluminum Perovskite

Bibliography

[1] A. Del Guerra et al. *"State of the art of PET, SPECT and CT for small animal imaging"*, Nucl. Instrum. Meth A **583** (2007) 119.

[2] S. Agostinelli et al., *"GEANT4 a simulation toolkit"*, NIM A **506** (2003) 250.

[3] F.F. Knapp, Cancer Biother Radiopharm. **13** (1998) 337.

[4] A. Antoccia et al., Nucl. Phys. B (Proc. Suppl.) **150** (2006) 411.

[5] J.S. Wang et al., Eur. J. Nucl. Med. **23** (1996) 13.

[6] M. Nicolini, U. Mazzi, *"Technetium, Rhenium and other Methals in Chemistry and Nuclear Medicine"*, SGEditoriali, Padova **6** (2002) 689.

[7] M.C. Giron et al., *"YAP-Camera Device for Biodistribution Studies in Mice of ^{99m}Tc- Radiotracers"*, Poster at the 6th Int. Symp. on Technetium in Chemistry and Nuclear Medicine, Brixen, (2002).

[8] A. Antoccia, et al., *"188-Rhenium induced cell death and apoptosis in a panel of tumor cell lines"*, Nucl. Instrum. Meth. A **571** (2007) 471.

[9] R.R. Weichselbaum, W. Dahlberg, J. Little, Proc. Natl. Acad. Sci. USA **82** (1985) 4732.

[10] B. Zhivotovsky, B. Joseph, S. Orrenius, Exp. Cell Res. **248** (1999) 10.

[11] O. Nagano, H. Sava, Cancer Sci. **95** (2004) 930.

[12] `http://www.nucleide.org/DDEP_WG/Nuclides/Re-188_tables.pdf`

[13] A. Antoccia et al. *Preliminary data on DNA damage and biodistribuition by* ^{188}*Re "in vitro" and "in vivo" systems.* Poster Session - Micros 2005, 14^{th} Symposium on Microdosimetry, November 13 - 18 2005, Venice (Italy).

[14] J.A. Jacquez: *"Compartmental Analysis in Biology and Medicine"*, BioMedware, Ann Arbor (1996).

[15] C. Cobelli, D. Foster, G. Toffolo: *"Tracer Kinetics in Biomedical Research"*, Kluwer, New York (2000).

[16] Mosmann T. *"Rapid colorimetric assay for cellular growth and survival: application toproliferation and cytotoxicity assays."* J Immunol Methods. **95** (1983) 55.

[17] P.K. Sneed et al. Int. J. Radiat. Oncol. Biol. Phys. **29** (1994) 719.

[18] Y. Gavrieli, Y. Sherman, Ben-Sasson SA. J Cell Biol. **119** (1992) 493.

[19] L. Beaulieu et al., *"Overview of GEANT4 applications in medical physics"*, Proceedings of IEEE-NSS **3** (2003) 1743.

[20] `http://reat.space.qinetiq.com/gps/new_gps_sum_files/gps_sum.htm`

[21] `http://proj-clhep.web.cern.ch/proj-clhep/manual/RefGuide/`

[22] `http://proj-clhep.web.cern.ch/proj-clhep/manual/RefGuide/#rand`

[23] F.James, Comp. Phys. Comm. **60** (1990) 329.

[24] M. J. Berger, *"Monte Carlo Calculation of the penetration and diffusion of fast charged particles"*, in Methods in Comput. Phys. **1** (1963) 135.

[25] `http://www.ge.infn.it/geant4/lowE/`

[26] `http://www.llnl.gov/cullen1/photon.htm`

[27] `http://www.llnl.gov/cullen1/electron.htm.`

[28] `http://www.llnl.gov/cullen1/atomic.htm.`

[29] J. Apostolakis et al., *"GEANT4 low energy electromagnetic models for electrons and photons"*, CERN-OPEN-99-034 (1999).

[30] J. Tuli, *"Evaluated Nuclear Structure Data File"* BNL-NCS-51655- Rev87, (1987).

[31] Chapter 25, GEANT4 Physics Reference Manual.

[32] A. Perrotta et al. *"A YAP camera for the biodistribution of* ^{188}*Re conjugated with Hyaluronic-Acid in "in vivo" systems."* Nucl. Instrum. Meth. A **571** (2007) 484.

[33] F. de Notaristefani et al., Eur. J. Nucl. Med. **22** (1995) 337.

[34] A. Del Guerra et al. *"Measurement of absolute light yield and determination of a lower limit for the light attenuation length for YAP:Ce crystal."* IEEE Trans. Nucl. Sci. **44** (1997) 2415.

[35] CRYTUR, Preciosa a.s., Palackeho 175, 51119 Turnov, Czech Republic.

[36] `http://www.hamamatsu.com`

[37] `http://www.nuclearfields.com`

[38] `http://www.ni.com`

[39] N.Uzunov, et al., LNL Ann. Rep., LNL-INFN(REP), 207/05.

[40] `http://www.novarad.com/documents/MPX.PDF`

[41] R. Pani et al., *"Lanthanum scintillation crystals for gamma ray imaging"*, Nucl. Instrum. Meth. A **567** (2006) 294.

[42] U. Mazzi et al. *"Biokinetic and Dosimetric Studies OF ^{188}Re-Hyaluronic Acid: A New Radiopharmaceutical For Treatment Of Hepatocellular Carcinoma"*, to be published on Nuclear Medicine and Biology.

[43] Anger H. O., *"Scintillation Camera"*, Rev. Sci. Instrum. **29** (1958) 27.

[44] Sanchez et al., *"Performance tests of two portable mini gamma cameras for medical applications"*, Med. Phys. **33** (2006) 4210.

[45] A. Nassalski, M. Kapusta, T. Batsch, D. Wolski, D. Muckel, W.Enghardt, and M. Moszyski, *"Comparative Study of Scintillators for PET/CT Detectors"*, IEEE Trans. Nucl. Sci. **54** (2007) 3.

[46] `http://www.bicron.com`

[47] R. Pani et al. *"High Spatial and energy resolution gamma imaging based $LaBr_3$:Ce continuos crystals"*, NSS-MIC IEEE 2008 Dresden, Abstract 2704.

[48] F. Sanchez et al. *"Design and tests of a portable mini gamma camera"*, Med. Phys. **31** (2004) 1384.

[49] G.F. Knoll, *"Radiation Detection and Measurement"*, John Willey and Sons Press. USA, 1979.

[50] M. Moszyski et al. *"Study of $LaBr_3$ Crystals Coupled to Photomultiplier and Avalache Photodiodes"*, IEEE NSS-MIC Conference Record **2** (2007) 1351.

[51] P. Iredale, *"The effect of the non-proportional response of NaI:Tl crystals to electrons upon the resolution for gamma-rays"*, Nucl. Instrum. Meth. A **11** (1961) 340.

[52] M. Moszynski et al, *"Intrinsic energy resolution of NaI:Tl"*, Nucl. Instrum. Meth. A **484** (2002) 259.

[53] G. Bizarri et al: *"Scintillation properties of $\emptyset 1\times 1$ inch^3 Labr$_3$:5%Ce^{3+} crystal"*, IEEE Trans Nucl. Sci. **53** (2006) 615.

[54] F. Salvat, J. M. Fernandez-Varea, E. Acosta, and J. Sempau, *"PENELOPE: A code system for MonteCarlo simulation of electron and photon transport"* Workshop Proceedings, OECD Nuclear Energy Agency, Issy-les-Moulineaux, (2001) ISBN: 92-64-18475-9.

[55] A. Levin and C. Moisan, *"A More Physical Approach to Model the Surface Treatment of Scintillation Counters and its Implementation into DETECT"*, NSS Conference Record **2** (1996) 702.

[56] `http://en.wikipedia.org/wiki/List_of_refractive_indices`

[57] `http://en.wikipedia.org/wiki/Direct_current#Various_definitions`

[58] R. Carotenuto et al. *"Fast scanning probe for ophthalmic echography using an ultrasound motor."* Ultrasonics, Ferroelectrics and Frequency Control, IEEE Trans Nucl. Sci. **52** (2005) 2039.

[59] P. Bennati *"Design and development of a dual-modality ultrasound/SPET system"*, Scuola di Specializzazione in Fisica Sanitaria - Physics Dpt. "Sapienza" University of Rome - thesis 2008.

[60] Kim H, Furenlid L R, Crawford M J, Wilson D W, Barber H B, Peterson T E, Hunter W C J, Liu Z, Woolfenden J M, Barrett H H. *" A small-animal single-photon emission computed tomography (SPECT) imager based on eight cadmium zinc telluride (CZT) detector arrays"* Med. Phys. **33** (2006) 465.

[61] M. A. Lodge, S. Webb, M. A. Flower, and D. M. Binnie, *"A protopyte rotating slat collimator for single photon emission computed tomography"*, IEEE Trans. Med. Imag. **15** (1996) 500.

[62] S. Dale et al. *"A mobile tomographic gamma camera system for acute studies"* IEEE Trans Nucl. Sci. **44** (1997) 199.

[63] G. Bal et al., IEEE Trans Nucl. Sci. **53** (2006) 2619.

[64] `http://geant4.web.cern.ch/geant4/support/index.shtml`

[65] `http://www.physics.ubc.ca/~mirg/home/tutorial/fbp_recon.html`

[66] E. Hecht and A. Zajac. *"Optics"* Addison-Wesley Publishing Co. 1974 pp. 71-80 and pp. 244-246

[67] G.F. Knoll, T.F. *"Light Collection Scintillation Detector Composites for Neutron Detection"*, IEEE Trans. Nucl. Sci. **35** (1988) 872.